Polystyrene nanoplastics as an ecotoxicological hazard: cellular and transcriptomic evidences on marine and freshwater *in vitro* teleost models

P.R. Saraceni [a,1], A. Miccoli [b,1], A. Bada [c], A.R. Taddei [d], M. Mazzonna [e], A.M. Fausto [c], G. Scapigliati [c], S. Picchietti [c,*]

[a] *Italian National Agency for New Technologies, Energy and Sustainable Development (ENEA), Department of Sustainability, 00123 Rome, Italy*
[b] *National Research Council, Institute for Marine Biological Resources and Biotechnology (IRBIM), 60125 Ancona, Italy*
[c] *Dept. for Innovation in Biological, Agro-food and Forest systems (DIBAF), University of Tuscia, Largo dell'Università snc, 01100 Viterbo, Italy*
[d] *Center of Large Equipments, Section of Electron Microscopy, University of Tuscia, Largo dell'Università Snc, 01100 Viterbo, Italy*
[e] *National Research Council, Institute for Biological Systems (ISB), 00015 Monterotondo, Italy*

HIGHLIGHTS

- PS-NPs were uptaken and translocated by RTG-2 and SAF-1 cells.
- Morphological and viability impacts were identified.
- SAF-1 had a 4-fold higher cytotoxic sensitivity than RTG-2.
- SAF-1 suffered extensive programmed cell death in response to 20 nm PS-NPs.
- Functional analyses in SAF1 reported transcriptional changes at sublethal and lethal 20 nm PS-NPs doses.

GRAPHICAL ABSTRACT
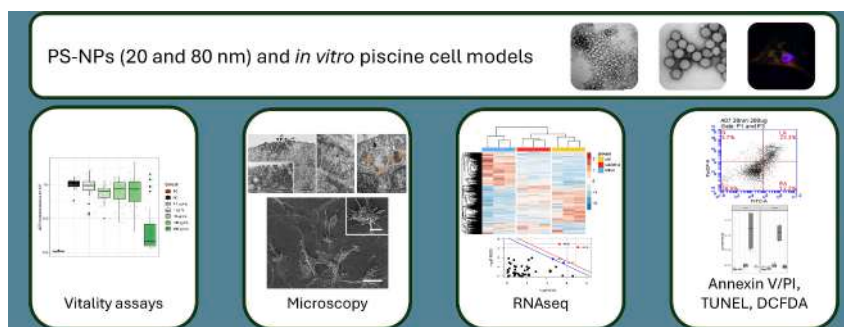
ARTICLE INFO

ABSTRACT

The contamination of marine and freshwater environments by nanoplastics is considered a global threat for aquatic biota. Taking into account the most recent concentration range estimates reported globally and recognizing a knowledge gap in polystyrene nanoplastics (PS-NPs) ecotoxicology, the present work investigated the harmful effects of 20 nm and 80 nm PS-NPs, at increasing biological complexity, on the rainbow trout *Oncorhynchus mykiss* RTG-2 and gilthead seabream *Sparus aurata* SAF-1 cell lines. Twenty nm PS-NPs exerted a greater cytotoxicity than 80 nm ones and SAF-1 were approximately 4-fold more vulnerable to PS-NPs than RTG-2. The engagement of PS-NPs with plasma membranes was accompanied by discernible uptake patterns and morphological alterations along with a nuclear translocation already within a 30-min exposure. Cells were structurally damaged only by the 20 nm PS-NPs in a time-dependent manner as indicated by distinctive features of the execution phase of the apoptotic cell death mechanism such as cell shrinkage, plasma membrane blebbing, translocation of phosphatidylserine to the outer leaflet of the cell membrane and DNA fragmentation. At last, functional analyses unveiled marked transcriptional impairment at both sublethal and lethal doses of 20 nm PS-NPs, with the latter impacting the "Steroid biosynthesis", "TGF-beta signaling pathway", "ECM-receptor

* Corresponding author.
 E-mail address: picchietti@unitus.it (S. Picchietti).
[1] These authors contributed equally to the manuscript.

interaction", "Focal adhesion", "Regulation of actin cytoskeleton" and "Protein processing in endoplasmic reticulum" pathways. Overall, a distinct ecotoxicological hazard of PS-NPs at environmentally relevant concentrations was thoroughly characterized on two piscine cell lines. The effects were demonstrated to depend on size, exposure time and model, emphasizing the need for a comparative evaluation of endpoints between freshwater and marine ecosystems.

1. Introduction

Global plastic production increased to 403 Mt in 2022[2] and is projected to double in 20 years and to triple by 2060 (Lebreton and Andrady, 2019; OECD, 2023). Most plastic waste isn't properly managed, with only 9 % recycled, 19 % incinerated, and the rest ending up in landfills or uncontrolled dumpsites (Kibria et al., 2023), contributing to the accumulation into the environmental compartments such as air, soil, seas and oceans (Du et al., 2022; Guo et al., 2020; Kibria et al., 2023; Li et al., 2021; OECD, 2023; X. Zhao et al., 2023).

Marine ecosystems bear the brunt of plastic debris (García Rellán et al., 2023; Law, 2017). More than 171 trillion plastic particles are estimated to accumulate in the marine environment (Eriksen et al., 2023) and undergo biological, physical and chemical degradation resulting into smaller sizes. Polystyrene i) is one of the most commonly non-biodegradable fabricated polymer that contributes to a significant fraction of environmental plastic pollution (de Haan et al., 2019; Sendra et al., 2021; Turner, 2020), ii) lists among the most reported polymers in marine biota (de Sá et al., 2018) and iii) exhibits significantly higher toxicity compared to all other tested polymers (Yang and Nowack, 2020). Recently, nanoplastics (NPs), whose sizes are smaller than 1000 nm (Gigault et al., 2018), have gained attention due to their ability to cross biological membranes such as the intestinal and blood brain barriers, increasing their potential toxicity towards marine organisms (Feng et al., 2023; Khan and Jia, 2023; Peng et al., 2020; Zhu et al., 2023). NPs may induce cytotoxicity, neurotoxicity, genotoxicity, oxidative stress, alteration of metabolism, inflammation and developmental malformations in marine species (Gonçalves and Bebianno, 2021; Han et al., 2022; Kik et al., 2020; Yong et al., 2020; Zaki and Aris, 2022), but the cellular and molecular mechanisms behind the impacts remain not fully understood.

Teleost-derived cell lines are increasingly employed as research tools (Goswami et al., 2022; Hernández-Moreno et al., 2022). These are considered relevant *in vitro* models in toxicological studies aimed at investigating the effects of several environmental pollutants including NPs (Bols et al., 2005; Hernández-Moreno et al., 2022; Revel et al., 2021). In addition, the use of established cell lines ensures a high reproducibility of experimental data and allows high throughput approaches, aiding regulatory efforts (Moné et al., 2020; Wange et al., 2021). The piscine fibroblast-like RTG-2 and SAF-1 cell lines, derived from rainbow trout *O. mykiss* and gilthead seabream *S. aurata* respectively, were widely used in various fields (El Aamri et al., 2012; Bandín et al., 2006; Goswami et al., 2022; Kim et al., 2023; Lisser et al., 2017; Parra-Riofrio et al., 2023; Perez-Prieto et al., 1999; Pham et al., 2020; Valero et al., 2021; J. Z. Zhao et al., 2023), including ecotoxicology (Bermejo-Nogales et al., 2017; Boháčková et al., 2023; Fent, 2001; Galbis-Martínez et al., 2018; Hernández-Moreno et al., 2022; Ruiz et al., 2020). For these reasons, this study investigated the toxicological effects induced by 20 nm and 80 nm polystyrene nanoplastics (PS-NPs) on RTG-2 and SAF-1 cell lines. We employed an *in vitro* approach at increasing complexity to i) evaluate the dose, time and size-dependent cytotoxic potential of PS-NPs, ii) dissect the processes of PS-NPs uptake, cellular component interactions and their morphological impacts and iii) profile the cell transcriptional responses and molecular mechanisms via high-throughput RNAseq functional analysis, with the aim of characterizing

their effects on two piscine models, ultimately filling gaps in the ecotoxicology of environmentally-relevant PS-NPs concentrations.

2. Methods

2.1. Oncorhynchus mykiss gonad tissue (RTG-2) and Sparus aurata fin-1 (SAF-1) cell culture

RTG-2, a cell line exhibiting fibroblast morphology, was isolated from the ovary of rainbow trout *Oncorhynchus mykiss* (Wolf and Quimby, 1962). Optimal conditions for culture growth were achieved at 22 °C in Leibovitz's L-15 supplemented with 2 mM L-glutamine, 100 U/mL penicillin, 100 μg/mL streptomycin and 30 % inactivated fetal bovine serum (FBS).

SAF-1 cell line (ECACC 00122301) is a continuous fibroblast-like culture established from gilthead seabream *Sparus aurata* caudal fin (Bejar et al., 1997). Optimal conditions for culture growth were achieved at 22 °C in L-15 medium (Life Technologies) supplemented with 1 % L-glutamine, 100 U/mL penicillin, 100 μg/mL streptomycin and 10 % inactivated FBS. Medium osmolarity was adjusted to seabream serum (355 mOsm/kg) using 3 M NaCl.

Both lines were routinely cultivated in 75 cm² tissue culture flasks (Jet Bio-Filtration Co.), and the subculture and medium renewal occurred once per week.

2.2. Characterization of PS-NPs by TEM, DLS and DELS

Pristine PS-NPs used in this study were either non-fluorescent (sizes of 20 and 80 nm, cat. # 3020A and 3080A, Thermo Scientific™) or fluorescent (sizes of 20 and 75 nm, ex./em. 468/508 and 542/612, respectively, cat. # R25 and G75 Fluoro-Max Thermo Scientific™). Non-fluorescent beads were used for cytotoxicity assays, ultrastructural analysis, transcriptomics, elucidation of cell death pathway and reactive oxygen species (ROS) quantification; fluorescent PS-NPs were used for cellular uptake experiments.

2.2.1. Negative staining procedure

The ultrastructure of PS-NPs was characterized by negative staining. They were sonicated for 10 min at the Sonica 2200 MD 53 sonicator (Soltec), then diluted in sterile milliQ water at a final concentration of 200 μg/mL and sonicated once again for 30 s. Afterwards, 10 μL of each sample were allowed to adsorb for a few minutes on copper grids coated with formvar and carbon. After removal of excess liquid, the grids were placed on a first drop of 2 % uranyl acetate in water for 10 s, and on a second drop for 2 min. After washes with double-distilled H₂O, samples were left to dry and then observed under a transmission electron microscope (TEM) Jeol 1200 EX II equipped with a CCD camera Olympus SIS Veleta (CGA, section of Electron Microscopy). Image acquisition and PS-NPs diameter measurements were performed using the iTEM software.

2.2.2. Dynamic and Dielectrophoretic Light Scattering measurements

Hydrodynamic diameter (D_h), polydispersity index (PDI) and ζ-potential value of commercial PS-NPs were investigated by Dynamic and Dielectrophoretic Light Scattering measurements (DLS, DELS) using a Zetasizer Nano ZS (Malvern Instruments) equipped with a 5 mW He/Ne laser (λ = 632.8 nm) and a thermostatted cell holder. Temperature was set constantly at 25 °C. Particle size and PDI were measured by DLS in

backscatter detection, at an angle of 173°. The measured autocorrelation function was analyzed by using the cumulant fit. The first cumulant was used to obtain the apparent diffusion coefficients D of the particles, further converted into apparent Dh by using Stokes-Einstein equation:

$$D_h = \frac{K_b T}{3\pi\eta D}$$

where $K_b T$ is the thermal energy and η is the solvent viscosity.

The ζ-potential of PS-NPs was determined from the electrophoretic mobility (μ) by DELS measurements. Analysis of the Doppler shift to assess the electrophoretic mobility was done by using phase analysis light scattering (PALS). The mobility μ of PS-NPs was converted into a ζ-potential using the Smoluchowski equation:

$$\zeta = \frac{\mu\eta}{\varepsilon}$$

where ε and η are the permittivity and the viscosity of the solution, respectively. PS-NPs were diluted to a concentration of 100 μg/mL in distilled water or L-15 medium in presence or absence of 10 or 30 % FBS, then sonicated for 30 s prior DLS analysis. Hydrodynamic diameter, PDI and ζ-potential reported correspond to the average of three different measurements.

2.3. ATP detection assay

Cell viability following PS-NPs exposure was determined by measuring the intracellular adenosine triphosphate (ATP) levels using the luciferase-based ATPlite assay (PerkinElmer, Waltham, MA, USA), which allows the assessment of cytocidal, cytostatic and proliferative effects. Based on preliminary assays evaluating growth rate and optimal absorbance readings, RTG-2 and SAF-1 cell lines were seeded in 96-well microplates (ViewPlate, Perkin Elmer) at a density of $8 * 10^3$ cells per well in 100 μL of L-15 medium. Cells were exposed to five doses of the 20 nm and 80 nm PS-NPs up to the lowest lethal one (i.e. 0.1, 1, 10, 100 and 200 μg/mL) for 0.5, 6 and 24 h. Two additional doses, i.e. 400 and 800 μg/mL, were required for RTG-2 to identify the actual cytotoxic dose. As a negative control, cells were grown in L-15 medium; as a positive control, cells were added of NaN_3 0.5 % v/v. At each experimental time point, cells were lysed and the amount of emitted light, linearly correlated with ATP quantity, was measured at a microplate luminometer (Victor2™, PerkinElmer) for 10 min in the dark. Six replicates per each PS-NPs dose were performed. Cytotoxicity of the treated experimental groups was normalized to the negative control and expressed as mean ± SEM.

2.4. Transmission Electron Microscopy (TEM)

RTG-2 and SAF-1 were cultured for 24 h on sterile PET track-etched membranes (Falcon) inserted in 24-well cell culture plates (Falcon) at a density of $4 * 10^4$ cells per well, then treated with 800 and 200 μg/mL (i. e. cytotoxic doses) of 20 nm or 80 nm PS-NPs, respectively, for 0.5, 6 and 24 h. After the treatment, cells were fixed overnight at 4 °C with 2.5 % paraformaldehyde and 2 % glutaraldehyde in 0.1 M cacodylate buffer at pH 7.2 and 0.075 % ruthenium red. Samples were washed with cacodylate buffer and post-fixed for 1 h at 4 °C with 2 % osmium tetroxide (OsO_4) and 0.075 % ruthenium red in 0.1 M cacodylate buffer at pH 7.2. After washing in distilled water, the samples were incubated with 0.5 % uranyl acetate for 0.5 h and then dehydrated in graded series of acetone and embedded in LR white resin (Agar Scientific). Ultrathin sections (60–80 nm) were stained with 1 % uranyl acetate and Reynolds lead citrate and then observed by TEM (Jeol 1200 EX II). Micrographs were acquired by the Olympus SIS Veleta CCD camera equipped with the iTEM software.

2.5. Confocal laser scanning microscopy (CLSM)

RTG-2 and SAF-1 were seeded in sterile poly-ʟ-lysine-coated glass coverslips (Menzel Glaser) inserted in 24-well plates at a density of 4 * 10^4 cells per well for 24 h. Then, a mixture of red fluorescent 20 nm PS-NPs (400 and 100 μg/mL, respectively) and green fluorescent 80 nm PS-NPs (400 and 100 μg/mL, respectively) was added for 0.5 and 6 h. As a negative control, cells were incubated in L-15 medium. After treatments, cells were washed twice with phosphate buffered saline (PBS) and fixed with 4 % PFA (Sigma-Aldrich) at 25 °C for 15 min. Cells were then washed twice with PBS and coverslips were mounted onto microscope slides with Fluoroshield mounting medium with DAPI (Sigma-Aldrich). Cells were imaged at the confocal microscope LSM 710 (Carl Zeiss Microscopy GmbH, Jena, Germany) using the interfaced software ZEN 2010. Multiple optical slices, encompassing the entire volume of the cells, were taken at 300 nm intervals. All samples were photographed with the same microscope setup. Channels from Z-stack acquisitions were merged by maximum intensity projection using Image J.

2.6. Scanning electron microscopy (SEM)

RTG-2 and SAF-1 were seeded on sterile cell culture inserts (Corning™ Falcon™) in 24-well cell culture plates at a density of 4 * 10^4 cells per well for 24 h. Then, they were exposed to 800 and 200 μg/mL, respectively, of 20 nm and 80 nm PS-NPs for 0.5, 6 and 24 h. Negative controls were incubated in L-15. At the end of the treatment, cells were washed twice and fixed with 2 % paraformaldehyde and 2.5 % glutaraldehyde in 0.1 M cacodylate buffer at pH 7.2 at 4 °C for 3 h. Samples were washed three times with cacodylate buffer, then post-fixed for 1 h with 1 % OsO_4 in 0.1 M cacodylate buffer at pH 7.2 for 1 h at 4 °C. After different washing in distilled water, the samples were dehydrated by incubation in progressively increasing concentration of ethanol solutions and dried using the liquid carbon dioxide method in a Critical Point Dryer (Balzers Union CPD 020). At last, samples were gold-coated in a Sputter Coater (Balzer Union MD 010) and examined using a Jeol JSM 6010 LA (Tokyo, Japan).

2.7. Transcriptomics

2.7.1. RNA preparation and sequencing

SAF-1 were employed to investigate the broad transcriptional impact of sublethal (100 μg/mL, highest non-cytotoxic) and lethal (200 μg/mL, cytotoxic) doses of 20 nm PS-NPs at 24 hpi (hours post-incubation), as per the ATP detection assay results (see section III of Methods and II of Results). Negative controls consisted of SAF-1 cells at unperturbed optimal culture conditions. Three independent biological replicates per each experimental group were included.

At the end of the 24-h incubation, both adherent and suspended cells were washed twice in PBS, lysed with RNAzol® RT (Merck, catalog # R4533) and stored at −80 °C until RNA was extracted as per manufacturer's instructions. RNA integrity was evaluated on a 1 % agarose gel. RNA quality and concentration were assessed using the Take3 microplate on the BioTek Epoch2 microplate spectrophotometer (Agilent Technologies).

mRNA libraries were prepared with the Quant seq 3′-term kit (Lexogen) and sequenced on an Illumina NextSeq 500 platform with a 1 × 75 single-end strategy and a depth of 1 × 5 M reads per sample. These steps were outsourced to BMR Genomics (Padua, Italy).

2.7.2. RNAseq data processing

Raw sequencing data, deposited into the NCBI SRA database under the BioProject ID PRJNA1041099, were quality-checked with FastQC v. 0.12.0 and pre-processed with fastp v. 0.23.2. Trimmed reads were mapped to the annotated reference *S. aurata* genome available at Ensembl Genome Browser (fSpaAur1.1, GCA_900880675.1), release 109 (Feb. 2023), using STAR v. 2.7.10b. Expression values were estimated at

the gene level with RSEM v. 1.3.3 (Li and Dewey, 2011).

2.7.3. Differential gene expression and transcriptome functional analyses

Differentially expressed genes were identified by means of the negative binomial generalized linear model implemented by the R DESeq2 package v. 1.40.1 (Love et al., 2014), setting the control as reference level in each of the two pairwise comparisons i.e. sublethal/lethal doses vs. control. Raw estimated counts were normalized with the median of ratios method. To enhance statistical power of DEGs detection, a minimal pre-filtering step maintained only genes with at least 3 reads across groups. Independent filtering based on the mean of normalized counts was implemented with a false discovery rate (FDR) cutoff of 0.05, and genes displaying extreme outliers or below the low mean threshold were removed from the dataset. Log$_2$ fold changes were tested for significance using the Wald test with design "$\sim$ experimental-group" and the null hypothesis of no differential expression between contrast levels for each gene. Shrinked log$_2$ fold changes were generated with the apeglm package (Zhu et al., 2019) for visualization purposes. A Likelihood Ratio test was conducted on a reduced model with design "$\sim$1" and the null hypothesis of the above full model fitting as well as the reduced one. Gene clusters exhibiting similar expression patterns across experimental groups were identified with the DEGreport package v. 1.36 (Pantano, 2021).

Gene annotations of *S. aurata* gene name, gene ontology mapping and *Danio rerio* Ensembl gene identifiers were obtained from BioMart using the biomaRt package v. 2.56.0 (Durinck et al., 2009): "drerio_homolog_ensembl_gene" and "drerio_homolog_orthology_type" attributes were retrieved and only a one-to-one orthology mapping was maintained for downstream functional analysis (Miccoli et al., 2024). This strategy enabled the exploitation of GO, gene sets and pathway annotations of the greatest possible quality.

Functional analyses were performed using clusterProfiler v. 4.8.1 (Wu et al., 2021), ReactomePA v. 1.44.0 (Yu and He, 2016), enrichplot v. 1.20.0 (Yu, 2023) and pathview v. 1.40.0 (Luo and Brouwer, 2013).

Over-representation analyses of DEGs were conducted using *S. aurata* and *D. rerio* Gene Ontology (GO) annotations. Enriched GO terms resulting from the annotations of the two species were compared for methodological validation. In both cases, the background dataset (i.e. universe) of the hypergeometric test was represented by all of the genes tested for significance by DESeq2.

Gene Set Enrichment Analysis (Subramanian et al., 2005) on the KEGG database was run using *D. rerio* Entrez gene identifiers retrieved from the org.Dr.eg.db R package v. 3.17.0 (Carlson, 2023). The significance FDR threshold was set at 0.1, and genes were pre-ranked based on the sign(log$_2$FC) * ($-$log$_{10}$(p-value)) formula from Reimand et al. (2019).

A Signaling Pathway Impact Analysis (Tarca et al., 2009), combining evidence from over-representation analysis and the actual perturbation on a given pathway, was conducted using SPIA v. 2.52.0. Entrez ID-annotated DE genes and their log$_2$ fold changes, along with *D. rerio* pathway topology from up-to-date manually-retrieved KEGG xml datasets were used. The number of bootstrap iterations for computing the probability of pathway perturbation was set to 2000.

2.8. Annexin V and propidium iodide staining in flow cytometry

SAF-1 were seeded in 6-well plates at a density of 7 * 10^5 cells per well and treated with the lethal dose of 20 nm PS-NPs for 24 h. As a negative control, cells were grown in L-15 medium; as positive control, cells were incubated with 4 μg/mL puromycin. After the treatment, cells were trypsinized, washed twice with ice-cold PBS and incubated in 100 μL of 1× Annexin V-binding buffer containing 5 μL Annexin V-FITC (Life Technologies) for 15 min at 22 °C in the dark. Afterwards, cells were washed with ice-cold PBS and added of 100 μL of 1× Annexin V-binding buffer plus propidium iodide (1 μg/mL, Life Technologies) and immediately analyzed by flow cytometry (FCM) (BD Accuri™ C6 Plus Flow

Cytometer, BDBiosciences).

2.9. TUNEL assay

Terminal Deoxynucleotidyl-Transferase mediated dUTP Nick End Labeling (TUNEL) assay was performed on SAF-1 cells using DeadEnd™ Fluorometric TUNEL System (Promega, Madison, WI, U.S.A.). Cells were grown at a density of 4 * 10^4 on sterile glass coverslips inserted in 24-well cell culture for 24 h. Distinct biological replicates were treated with the lethal dose of 20 nm PS-NPs and monitored along the 0.5–24 hpi timeframe. Cells were then fixed in 4 % paraformaldehyde at 4 °C, permeabilized with 0.2 % Triton X-100, exposed to the equilibration buffer (DeadEnd Tunel system, Promega) for 10 min and, subsequently, incubated with the rTdT incubation buffer (Promega) at 37 °C for 1 h in the dark to allow the tailing of green fluorescent nucleotides to 3′-OH DNA ends. The reaction was stopped by adding the 2× SSC buffer (Promega). Finally, they were washed twice with PBS and coverslips were mounted onto microscope slides with Fluoroshield mounting medium plus DAPI (Sigma-Aldrich). Images were captured in bright-field and two channel fluorescence (360 nm/460 nm, 488 nm/509 nm) using Leica microscope LMD6 and the interfaced software LAS-X (Leica).

2.10. DCFDA cellular reactive oxygen species detection assay

Intracellular ROS were quantified by means of 2′,7′-dichlorodihydrofluorescein diacetate (DCFDA, Merck). SAF-1 were seeded on 96-well microplates at a density of 8 * 10^3 cells per well in 100 μL of L-15 medium. As a medium control, cells were grown in L-15; as a hydrogen peroxide control, cells were grown in L-15 and added of 20 mM hydrogen peroxide without DCFDA; as a negative control, cells were grown in L-15 and added of 25 μM DCFDA without hydrogen peroxide; as a positive control, cells were grown in L-15 and added of both 20 mM hydrogen peroxide and 25 μM DCFDA. The "Hydrogen peroxide control" and the positive control served as internal controls. Cells were treated with the lethal dose of 20 nm PS-NPs. The assay protocol consisted in cells being washed with PBS, lysed with PBS/Triton 0.1 % and, in all experimental groups except for medium and hydrogen peroxide controls, incubated with 25 μM DCFDA for 45 min in the dark. Emission wavelength was measured at 530 nm with a microplate luminometer (Victor II PerkinElmer) at 3 and 24 hpi in all groups. Six replicates were performed. Intracellular ROS production of each experimental group was expressed as a mean ± SEM of relative fluorescence units (RFU).

2.11. Statistical analyses

Data analysis was conducted in the RStudio environment, R version 4.3.0. Data manipulation and transformation, statistical tests and annotated data visualization were conducted with the tidyverse, rstatix, ggpubr and RColorBrewer packages.

Datasets were statistically analyzed with the non-parametric Kruskal-Wallis H test followed by the Wilcoxon rank sum test for pairwise comparison with the Holm-Bonferroni method for *p*-value adjustment and NC as reference group.

Raw technical replicates of the ATPlite and DCFDA assays were averaged within incubation time, PS-NPs dose and size, or within each experimental group, respectively. With regard to the former, biological replicates of PS-NPs-treated groups were normalized to the negative control, and scaled data (i.e. 0 to 1) was employed in statistical tests. As for the latter, statistical significance was determined with the null hypothesis of no difference in fluorescence (i.e. a proxy of ROS quantity). The LC50 parameter from the cytotoxicity assay was modeled by curve fitting using normalized data and the "dose-response - inhibition, variable slope" equation in GraphPad Prism v. 9. Fitting was performed with the least squares method. Best-fit LC50 values were compared between datasets using the extra sum-of-squares F test, with the null hypothesis of the parameter being equal in both cell models.

3. Results

3.1. Shape, size, aggregating behavior and charge of commercial PS-NPs

TEM observation allowed us to evaluate the shape and aggregation tendency of fluorescent (Fig. 1B, D, F, H) and non fluorescent (Fig. 1A, C, E, G) PS-NPs. The smallest (20 nm) displayed an irregular morphology, while the largest (80 nm) showed a regular round shape, and both tended to form aggregates (Fig. 1). D_h, PDI and the ζ-potential values of PS-NPs are reported in Table 1.

PS-NPs size distribution and PDI were investigated by DLS measurements. Results showed a narrow size distribution for all commercial PS-NPs diluted in water. The D_h was in line with the manufacturer's technical specifications and no major discrepancies were highlighted between fluorescent and non-fluorescent particles per size (i.e. 21.66 ± 0.05 vs. 23.98 ± 0.07, and 82.4 ± 0.8 vs. 86 ± 1 nm). For PS-NPs suspended in L-15 medium, a slight increase in size was observed with low PDIs (0.006–0.089), except for the 20 nm fluorescent PS-NPs, for which an aggregation phenomenon was observed immediately after dilution in the medium, with the formation of a heterogeneous population of aggregates that could not be measured (data not shown). It is worth noting that the same aggregation tendency was observed for 20 nm non fluorescent PS-NPs, but in this case, the aggregation phenomenon occurred much more slowly, leading to the formation of a single population with dimension of 103 ± 1 nm and a PDI of 0.20 ± 0.01 nm after 4 h of incubation in L-15 (data not shown). In L-15 medium supplemented with 10 % or 30 % FBS the formation of heterogeneous populations of aggregates was observed for both types of 20 nm PS-NPs, while 80 nm PS-NPs, both fluorescent and non, displayed a single population with a consistent increment in size and PDI values compared to those determined in water. ζ-Potential values were determined for PS-NPs in different media by electrophoretic mobility measurements using the phase analysis light scattering (PALS) whenever the system was found to be monodispersed by DLS analysis. Both PS-NPs sizes exhibited negative and quite high ζ-potential values in water, which became less negative in L-15 medium and further decreased in absolute value in L-15 supplemented with 10 % or 30 % FBS.

Table 1

Hydrodynamic diameter (Dh), polydispersity index (PDI) and ζ-potential of non-fluorescent PS-NPs (100 μg/mL) in water and L-15 medium. N.D.: data non determinable due to technical limitations imposed by aggregation behavior of PS-NPs.

| PS-NPs	Medium	Dh (nm)	PDI	ζ-Potential (mV)
20 nm	Water	23.98 ± 0.07	0.105 ± 0.007	−30 ± 1
20 nm	L-15	28 ± 1	0.089 ± 0.005	−24 ± 2
20 nm	L-15 + 10 % FBS	N.D.	N.D.	N.D.
20 nm	L-15 + 30 % FBS	N.D.	N.D.	N.D.
80 nm	Water	86 ± 1	0.006 ± 0.003	−53 ± 1
80 nm	L-15	85.4 ± 0.9	0.006 ± 0.002	−21 ± 2
80 nm	L-15 + 10 % FBS	152 ± 2	0.201 ± 0.005	−9.7 ± 2
80 nm	L-15 + 30 % FBS	135 ± 1	0.266 ± 0.006	−8.7 ± 0.4

3.2. The impact of PS-NPs on intracellular ATP content of piscine cell lines

Cytotoxicity of PS-NPs of 20 and 80 nm at increasing doses and along a 24-h exposure was evaluated at three time points on RTG-2 and SAF-1 models by monitoring intracellular ATP content (Figs. 2–3A–B).

The 0.5-h exposure to 20 nm PS-NPs exerted a statistically significant ATP increase in RTG-2 up to the dose of 200 μg/mL, with that of 100 μg/mL leading to an ATP content relative to the negative control of 1.74 ± 0.12 (median ± S.E.) (p-adjusted 5.28e-05), as opposed to SAF-1, where ATP contents were consistent among treated and control cells ($\chi^2_{(5)}$ = 7.122, p-adjusted = 2.12e-01, n = 141). At 6 hpi, opposite statistically significant variations were caused by the highest dose of 200 μg/mL: median ATP content relative to negative controls was 1.52 ± 0.12 (p-adjusted 9.00e-03) and 0.31 ± 0.06 (p-adjusted 1.16e-10) in RTG-2 and SAF-1, respectively. At 24 hpi, a general ATP increase was again recorded in RTG-2 ($\chi^2_{(5)}$ = 23.66, p-adjusted = 7.56e-04, n = 144), with as much as 1.62 fold change at 100 μg/mL (p-adjusted 3.00e-03), whereas ATP levels in SAF-1 were not affected up to 100 μg/mL, and those exposed to 200 μg/mL reached the lowest median ATP content of 0.16 ± 0.07 compared to negative control (p-adjusted 1.34e-06) (Fig. 2A). The dose of 200 μg/mL was therefore recognized as the lethal one for SAF-1. With the aim of detecting actual cytotoxic doses,
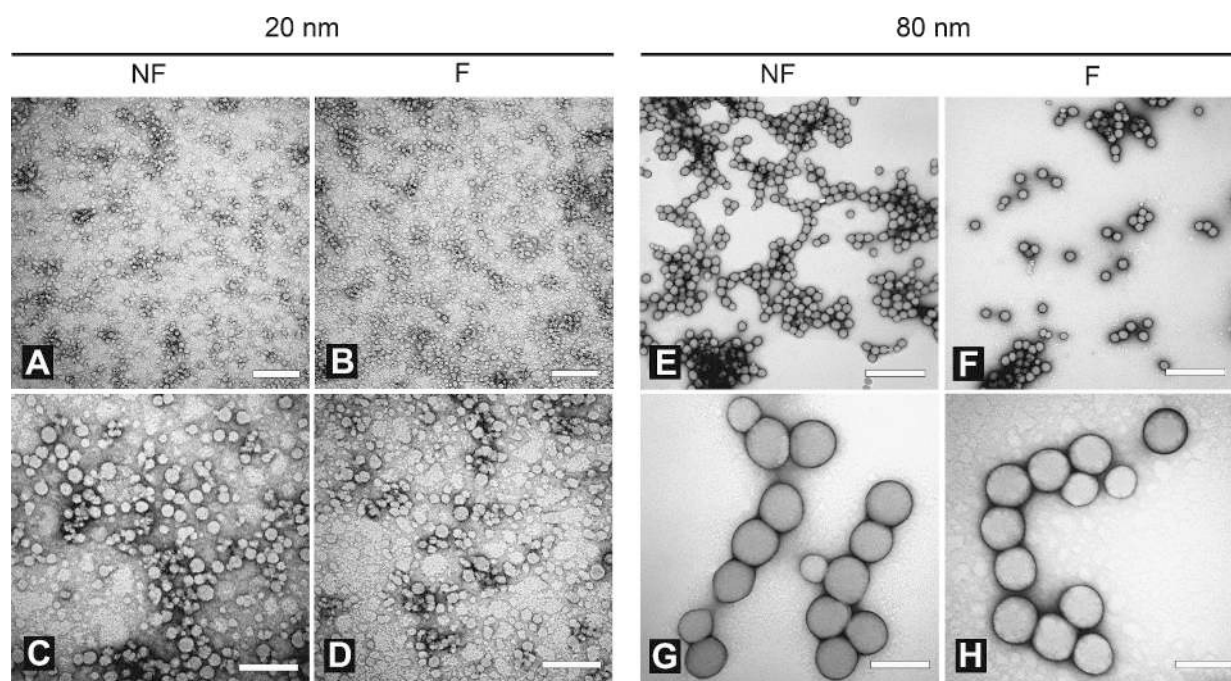
Fig. 1. Ultrastructural characterization by negative staining of 20 (A–D) and 80 (E–H) nm PS-NPs, either fluorescent (F) or non fluorescent (NF). Scale bars: A–B = 200 nm, C–D = 100 nm, E–F = 500 nm, G–H = 100 nm.
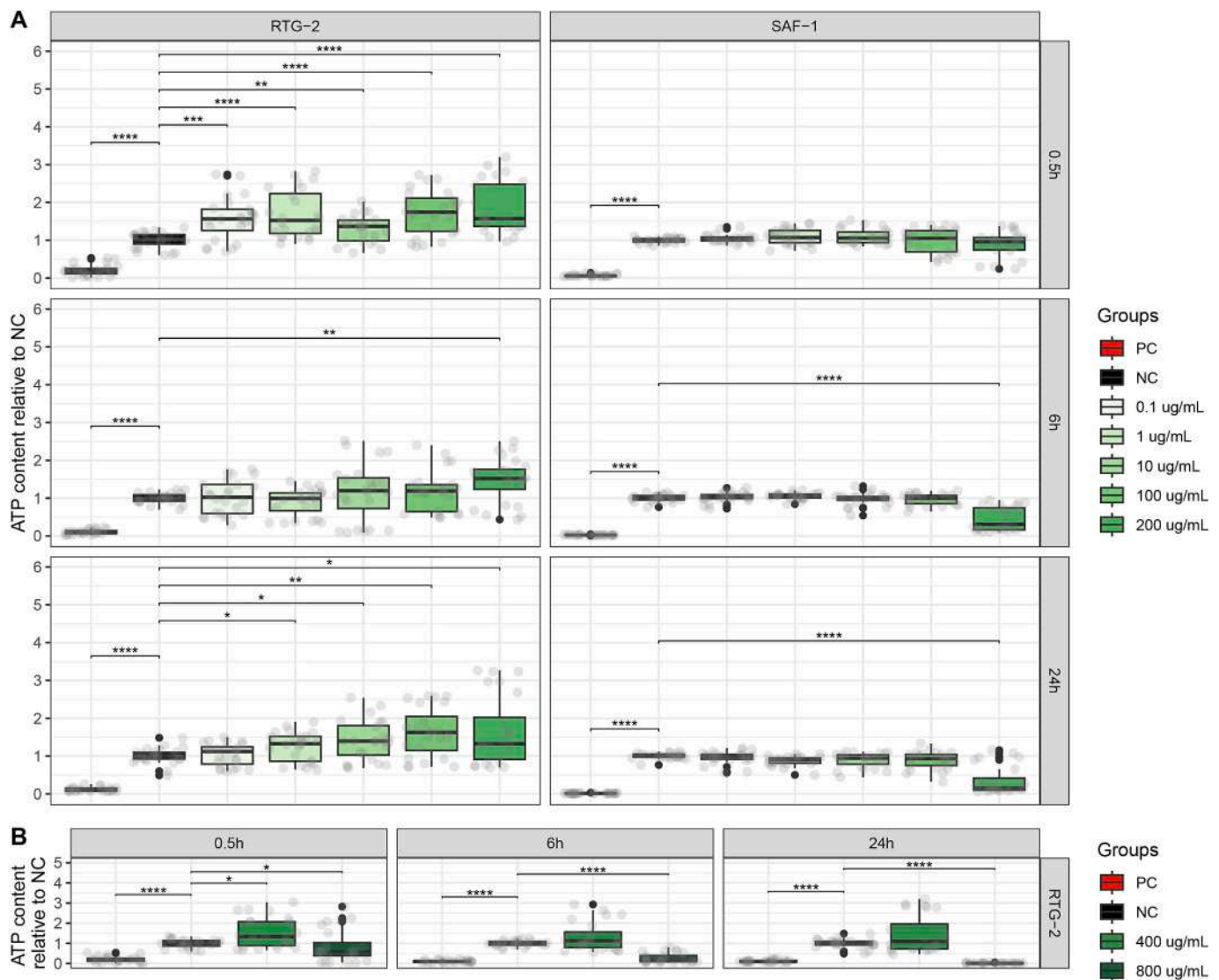
Fig. 2. RTG-2 and SAF-1 intracellular ATP levels as a proxy of cytotoxicity, expressed relatively to negative controls (i.e. undisturbed cells in growth media), following the 0.5-, 6- and 24-h exposure to 20 nm PS-NPs at 0.1, 1, 10, 100 and 200 μg/mL (A) and, only of RTG-2, to 400 and 800 μg/mL (B). PS-NPs sizes and doses are color-coded. Statistical significance according to the non-parametric Kruskal-Wallis H test followed by the Wilcoxon rank sum test for pairwise comparison. *: $p < 0.05$; **: $p < 0.01$; ***: $p < 0.001$; ****: $p < 1e-04$.

RTG-2 were exposed to 400 and 800 μg/mL and their effects evaluated at the same time points as above: the dose of 400 μg/mL induced a statistically significant impact consisting in a slight ATP increase only at 0.5 hpi (p-adjusted 2.3e-02), whereas a negative, time-dependent effect was always seen for the highest dose, leading to the lowest median ATP content relative to negative controls of 0.01 ± 0.003 (p-adjusted 2.48e-13) at 24 hpi (Fig. 2B). The LC50 at 24 hpi was ~478.9 and ~119.0 μg/mL for RTG-2 and SAF-1, respectively; these parameters differed significantly between cell models ($F_{(1,53)} = 20.07$, $p < 1e-04$). Cells exposed to 0.5 % v/v NaN$_3$ (positive controls) had a relative ATP content ranging from 0.096 to 0.18 (RTG-2) and from 0.013 to 0.06 (SAF-1).

With regard to 80 nm PS-NPs up to 200 μg/mL, a general increase in RTG-2 intracellular ATP content was observed at all three time points, with greatest median vitality indices of 2.04 at 0.5 hpi (100 μg/mL, p-adjusted 3.00e-03), 1.26 at 6 hpi (10 μg/mL, p-adjusted 2.88e-06) and 1.41 at 24 hpi (10 μg/mL, p-adjusted 3.90e-02). On the contrary, an impact was seen in SAF-1 already by 0.5 hpi at the highest dose of 200 μg/mL (0.79 ± 0.03, p-adjusted 3.98e-10). At 6 hpi no significative impacts were detected. At 24 hpi, the doses of 100 and 200 μg/mL induced a decreased vitality index of 0.85 ± 0.04 (p-adjusted 1.00e-02)

and 0.79 ± 0.03 (p-adjusted 7.15e-09) compared to controls (Fig. 3A). The two greatest doses tested on RTG-2 did not induce any cytotoxicity, and only that of 400 μg/mL increased ATP levels to 1.83 ± 0.17 at 0.5 hpi (p-adjusted 4.00e-03) (Fig. 3B). A dose-response curve could not be reliably fitted, and a LC50 therefore calculated, because 80 nm PS-NPs did not induce cytotoxicity to RTG-2 at any tested dose. Cells exposed to 0.5 % v/v NaN$_3$ had a relative ATP content ranging from 0.07 to 0.15 (RTG-2) and from 0.01 to 0.06 (SAF-1).

3.3. Cellular uptake and fate of negatively charged PS-NPs

A comprehensive ultrastructural analysis was conducted to obtain insights on PS-NPs interaction with RTG-2 and SAF-1 cell membranes, as well as their translocation and association with cellular components.

Fig. 4(A, D, G) show untreated RTG-2 cells exhibiting intact plasma membrane and nuclear envelope. Twenty nm PS-NPs were surrounded by a highly electron-dense material forming heterogeneous aggregates (as shown in Fig. 4B, E, H), and were efficiently internalized by RTG-2 cells. At 0.5, 6 and 24 h, 20 nm PS-NPs adhered on the cell surface (Fig. 4B and E, and upper insets), within the cytoplasm (Fig. 4H), and
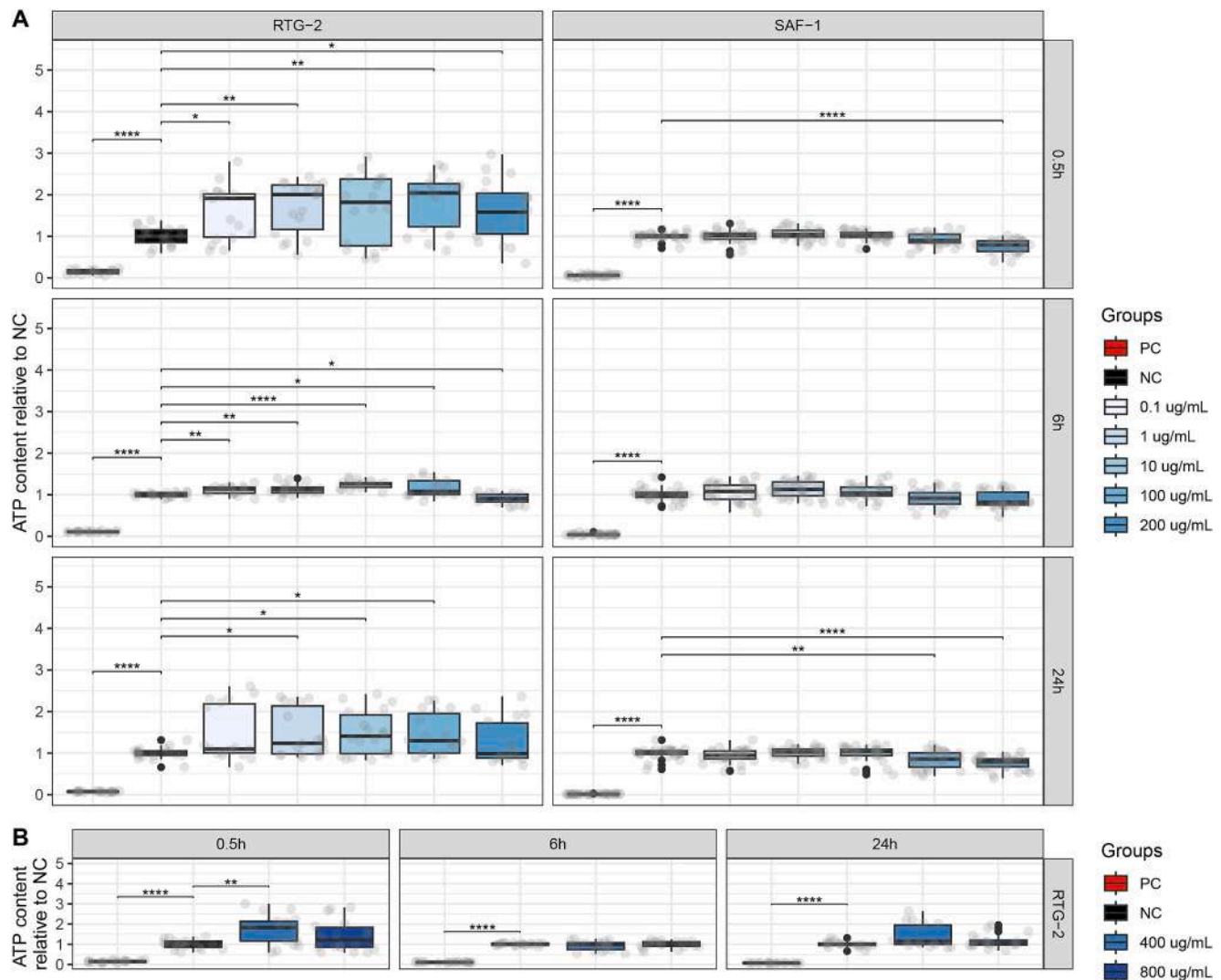
Fig. 3. RTG-2 and SAF-1 intracellular ATP levels as a proxy of cytotoxicity, expressed relatively to negative controls (i.e. undisturbed cells in growth media), following the 0.5-, 6- and 24-h exposure to 80 nm PS-NPs at 0.1, 1, 10, 100 and 200 μg/mL (A) and, only of RTG-2, to 400 and 800 μg/mL (B). PS-NPs sizes and doses are color-coded. Statistical significance according to the non-parametric Kruskal-Wallis H test followed by the Wilcoxon rank sum test for pairwise comparison. *: $p < 0.05$; **: $p < 0.01$; ***: $p < 0.001$; ****: $p < $ 1e-04.

inside the nucleus (insets of Fig. 4H), causing multiple ruptures in the plasma and nuclear membranes (insets of Fig. 4B, H). At all time points, an electron-dense halo surrounding 80 nm PS-NPs allowed for their clear visualization outside the cells (Fig. 4C), as well as their abundance within the cytoplasm (Fig. 4F). Notably, 80 nm PS-NPs moved to lysosomes and phagocytic vesicles (Fig. 4I). They were mostly localized in small discrete clusters in the perinuclear region.

Similarly to RTG-2, PS-NPs internalization in SAF-1 was evident at 0.5 and 6 hpi, coherently with confocal data. Untreated cells were devoid of any nanoplastics, presented undamaged plasma and nuclear membranes, and electron-lucent vesicles were occasionally present within the cytoplasm (Fig. 5A–B). At 24 hpi, 20 nm PS-NPs were clearly visualized due to their electron density and accumulated into the above-mentioned cytoplasmic vesicle (Fig. 5C–D). Eighty nm PS-NPs could be easily visualized in the cytoplasm, and were shown to interact with the membrane of such vesicles (Fig. 5F).

The combined internalization behavior was investigated by CLSM, demonstrating cytoplasmic uptake of both PS-NPs sizes already by 0.5 hpi in both cell models, indicated by green and red fluorescence (Fig. 6). Orthogonal vertical and horizontal stack views evidenced their trans-location to the DAPI-stained nuclei of both cell lines, revealed by cyan (i.

e. merge of blue and green channels) and magenta (i.e. merge of blue and red fluorescence) coloring. At 6 hpi, an accumulation of both PS-NPs size particles was observed in the cytoplasm, as revealed by an increase in red and green fluorescence, while 20 nm PS-NPs were predominant within the nucleus, as indicated by the magenta-colored fluorescence. RTG-2 and SAF-1 control cells were devoid of any fluorescent PS-NPs.

3.4. Morphological changes in PS-NPs treated cells: typical features of programmed cell death

Morphological changes in RTG-2 and SAF-1 models following PS-NPs exposure were observed by SEM.

With regard to RTG-2 (Fig. 7), both PS-NPs sizes altered cell morphology as early as 0.5 hpi with respect to untreated cells (Fig. 7A, D, G). Twenty nm and, particularly, 80 nm PS-NPs-treated cells exhibited a significant decrease in cell protrusions and loss of cell adhesion at all experimental times, reaching a maximum at 24 hpi (Fig. 7H–I). Eighty nm PS-NPs were confirmed to engage with and aggregate on cell membranes (insets of Fig. 7C, F, I), while 20 nm PS-NPs were demonstrated to cause cell membrane ruptures (Fig. 7E, inset).

As for SAF-1 (Fig. 8), the interaction between PS-NPs and cell surface
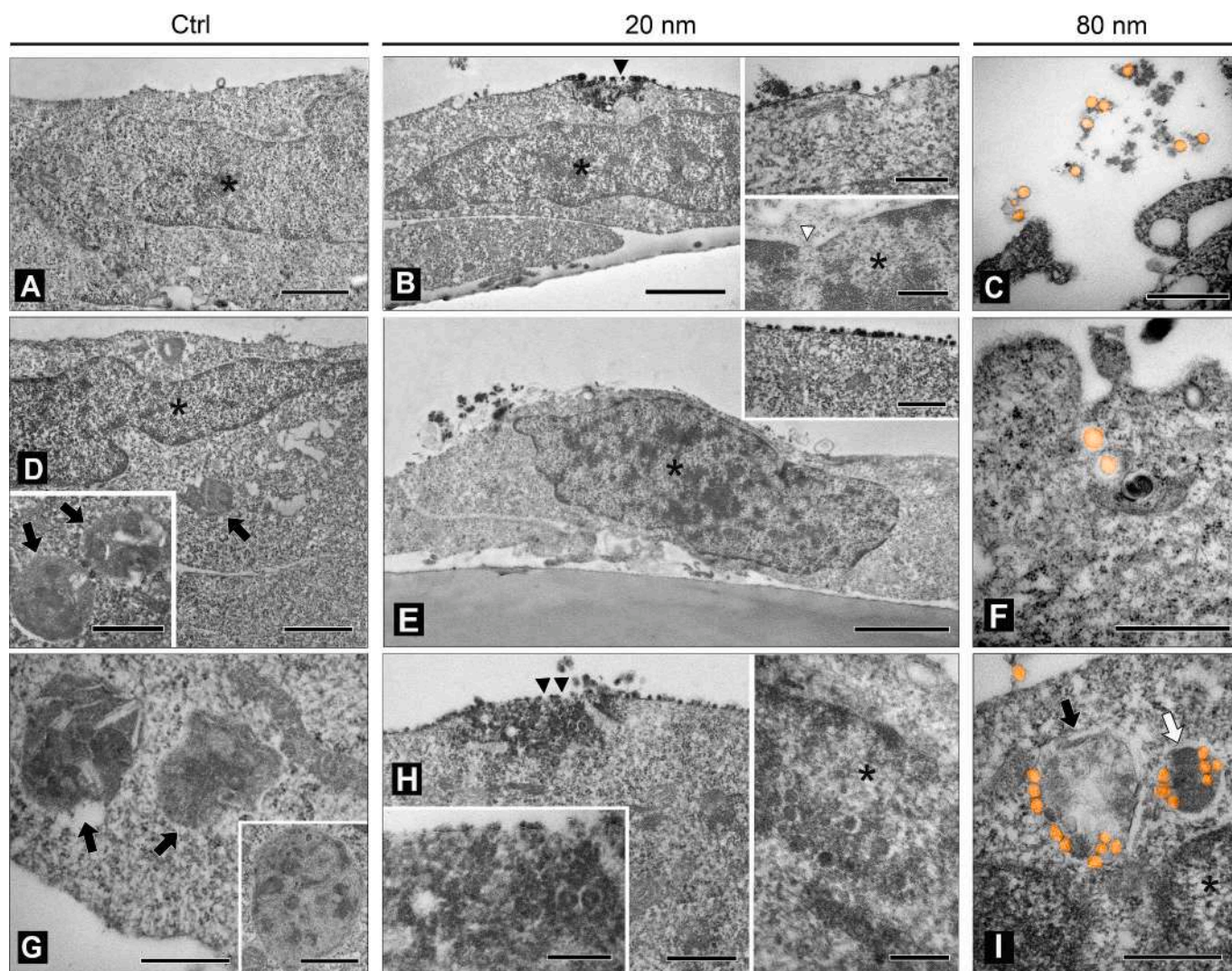
Fig. 4. Twenty and 80 nm PS-NPs internalization in RTG-2 cells along exposure times. Untreated cells (Ctrl) are shown in A, D and G; 20 nm PS-NPs-treated cells are shown in B, E and H; 80 nm particles-treated are shown in C, F and I. Eighty nm particles were highlighted in yellow. Scale bars: A = 1 μm; B = 1 μm, insets = 200 nm; C, F and I = 500 nm; D = 1 μm, inset D = 500 nm; E = 1 μm, inset E = 500 nm; G = 500 nm, inset G = 50 nm; H = 500 nm, insets = 200 nm; *: nucleus; black arrow: phagosome; white arrow: lysosome; black arrowhead: plasma membrane ruptures; white arrowhead: nuclear membrane rupture.

was confirmed as early as 0.5 hpi. Morphological modifications consisting in fusiform-shaped cells losing cell adhesion were observed following exposure to both PS-NPs sizes already by 0.5 hpi (Fig. 8B and inset). At 6, and more frequently at 24 hpi, 20 nm PS-NPs induced typical apoptotic features such as shrinkage and plasma membrane blebbing (Fig. 8E, H and inserts). Eighty nm PS-NPs did impact on the cell morphology, causing a reduction in cell protrusions determining a loss of adhesion in a time-dependent manner, but no typical apoptotic signatures were observed (Fig. 8C, F, I).

3.5. Transcriptomics and validating assays inspect the heightened sensitivity of SAF-1 cells to 20 nm PS-NPs

Taking into account the more severe cellular and morphological impacts imposed by PS-NPs on SAF-1 than RTG-2, transcriptomics, FCM, TUNEL and DCFDA assays were leveraged to unravel mechanistic information underlying PS-NPs toxicity in SAF1 cells.

### 3.5.1. Massive transcriptional changes were prompted by sublethal and lethal PS-NPs doses

A number of raw reads ranging between 7,153,793 and 10,405,871 across experimental groups was sequenced. Following quality-checking

and pre-processing, input reads for mapping onto the *S. aurata* genome accounted for 6,681,212–9,703,187. The percentage of uniquely mapped reads ranged from 73.16 % to 83.46 %, with an average mapped length of 73.55 nt. The percentages of reads unmapped due to read length issues were 12.25 %–22.60 %.

Expression data was produced for 27,714 genes. By maintaining only genes with a sum of raw read counts >2 across experimental groups, the dataset was reduced to 12,444 genes. By considering the 500, 1000 and 2000 genes associated with the greatest variance, a principal component analysis revealed a clear clustering of biological replicates within each experimental group, and the "experimental group" factor described 90 %, 87 % e 84 % of the variance, respectively (data not shown). A heatmap of correlations among regularized log-transformed counts confirmed a within-experimental group clustering and showed greater correlations between the control and the sublethal group: the lethal group was categorized in a distinct branch of the dendrogram (data not shown). A heatmap of the top 4000 genes sorted by greatest among−-treatment variance in counts is shown in Fig. 9A.

The likelihood ratio test-based differential expression (DE) analyses identified 2863 genes significantly changing in any direction across the three experimental groups. The two most abundant clusters encompassed genes exhibiting highest and lowest expression in the lethal <
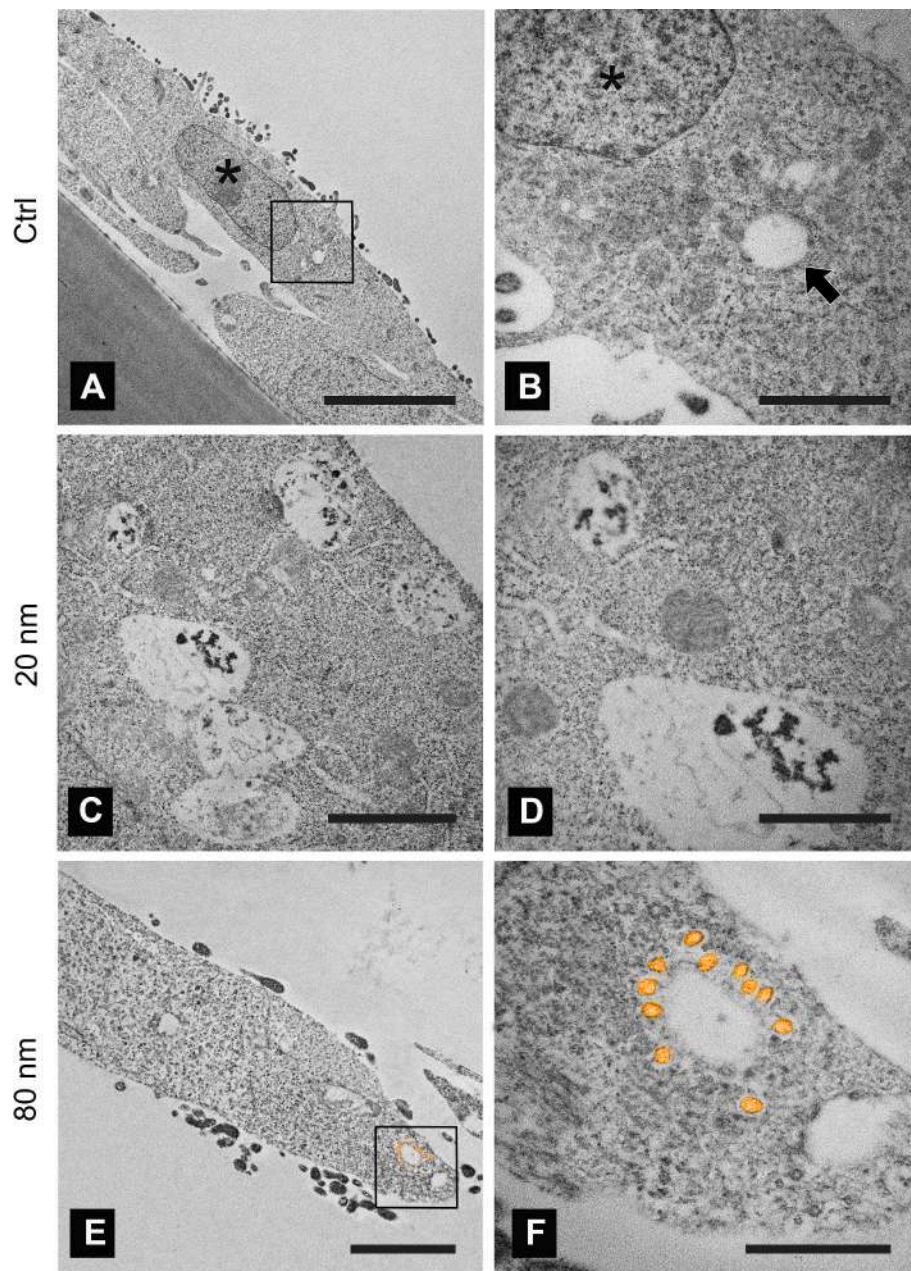
Fig. 5. Focus on 20 and 80 nm PS-NPs internalization in SAF-1 cells at 24 hpi. Untreated cells (Ctrl) are shown in A–B; 20 nm PS-NPs-treated cells are shown in C–D; 80 nm particles-treated cells are shown in E–F. Eighty nm particles were highlighted in yellow. Scale bars: A = 5 μm, B = 1 μm, C = 2 μm, D = 1 μm, E = 2 μm, F = 500 nm; *: nucleus; arrow: electron-lucent vesicle.

sublethal < ctrl groups (i.e. groups 2 and 1 of Fig. 9B, respectively).

The Wald test-based DE analysis identified 752 (sublethal vs. ctrl, from here on "sublethal" contrast; 420 up- and 332 down-regulated compared to the control group) and 3020 (lethal vs. ctrl, from here on "lethal" contrast; 1495 up- and 1525 down-regulated) (Fig. 9C) differentially expressed genes in Ensembl nomenclature. The greatest and lowest $\log_2$ fold change (FC) estimates in the sublethal and lethal contrasts were 6.83 and −3.54, and 8.02 and −7.93, respectively: the quartile distribution of $\log_2$ FCs per effect size direction is available in Table S1A–B. Eighty-one and 2349 DEGs were uniquely found in the sublethal and lethal contrasts, respectively, but 671 were shared between the two (Fig. 9D). Among these were genes involved in caveolin- or clathrin-mediated endocytosis and genes encoding for antioxidant enzymes, whose expression patterns are shown in Fig. 9E–F.

The 20 most differentially expressed genes sorted by lowest adjusted

p-value from the sublethal and lethal contrasts had a statistical support ranging from 1.35e−51 and 1.5e−13, and 3.29e−242 and 2.84e−48, respectively. Eight genes appeared as top 20 DEGs in both datasets, namely: *si:dkey-222f8.3*, predicted to enable endoribonuclease activity; *dusp5*, encoding for a protein belonging to the dual specificity protein phosphatase subfamily that negatively regulate members of the mitogen-activated protein (MAP) kinase superfamily (MAPK/ERK, SAPK/JNK, p38) associated with cell proliferation and differentiation; ENSSAUG00010015520, encoding for the cartilage intermediate layer protein 2-like containing a Mucin2_WxxW conserved domain, according to the best blastp hit; *marcksl1a*, encoding for a member of the myristoylated alanine-rich C-kinase substrate family, involved in cytoskeletal regulation as well as protein kinase C and calmodulin signaling; ENSSAUG00010018318, encoding for protein asteroid homolog 1-like containing the PIN (PilT N terminus) domain, presumably involved in
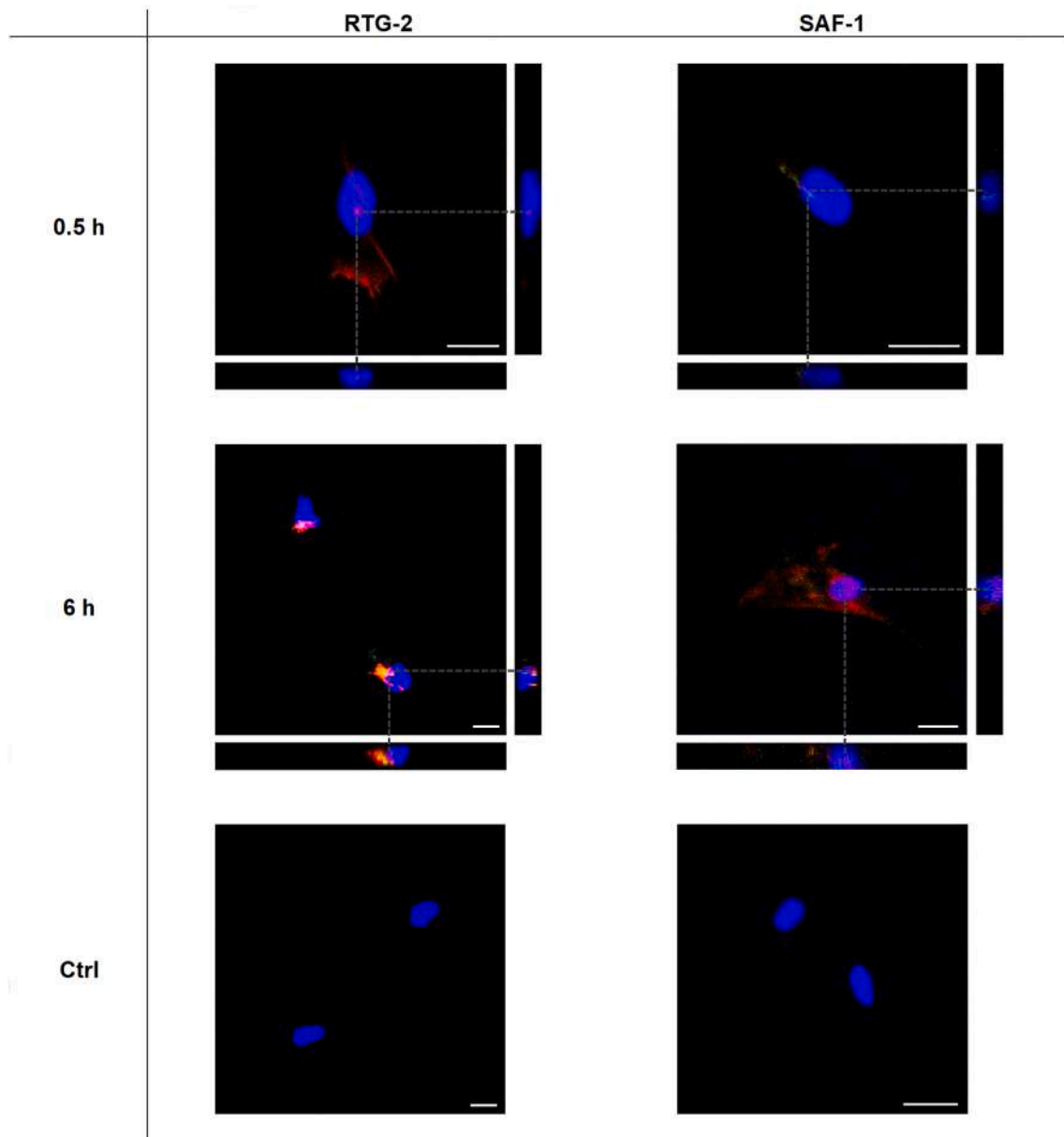
Fig. 6. Confocal analysis of 20 (red fluorescence) and 80 nm (green fluorescence) PS-NPs internalization at 0.5 and 6 h. A marked PS-NPs fluorescence was imaged in the perinuclear area and nucleus (DAPI) of cells. Scale bars = 10 μm.

nonsense mediated mRNA decay; *wsb2*, i.e. WD repeat and SOCS box containing 2, acting as substrate-recognition component of an E3 ubiquitin ligase complex that mediates the ubiquitination and subsequent proteasomal degradation of target proteins; *trib3*, tribbles pseudokinase 3, i) a negative regulator of NF-kappaB, ii) a sensitizer of cells to TNF- and TRAIL-induced apoptosis and iii) a negative regulator of the cell survival serine-threonine kinase AKT1; and *plin2*, i.e. perilipin 2, encoding for a protein entailed in intracellular lipid storage droplet coating. The complete lists of DEGs and of all genes tested for statistical significance for both contrasts are available in Table S2A–D, respectively.

Evidence of a greater number of, and a stronger statistical support for, genes involved in the intrinsic and/or extrinsic apoptotic pathways (Jan and Chaudhry, 2019) was found in the lethal than in the sublethal contras: i) ENSSAUG00010003126 ($\log_2$ FC 1.24, p-adj 1.80E-06), ENSSAUG00010003175 ($\log_2$ FC 1.21, p-adj 3.71E-06) and ENSSAUG00010023549 ($\log_2$ FC 0.61, p-adj 8.94E-05) only resulted DE within the lethal contrast: the first two encode for caspase-8-like, an

established and evolutionary conserved initiator of death receptor-mediated apoptosis (Sakata et al., 2007), the latter encodes for BAX (BCL2 associated X, apoptosis regulator), an apoptotic inducer through increased mitochondrial membrane permeability, cytochrome *c* release, and caspase-3 activation (Cance and Golubovskaya, 2008; Peña-Blanco and García-Sáez, 2018); ii) ENSSAUG00010003635, encoding for caspase-9, recruited and activated upon cytochrome *c* release from the mitochondria and downstream cleaving caspase-3, −6 or −7 (Kuida, 2000), was more expressed in the lethal ($\log_2$ FC 0.96, p-adj 2.26E-05) than in the sublethal contrast ($\log_2$ FC 0.58, p-adj 0.042); iii) the apoptotic network resulting from the lethal contrast displayed richer functional and physical protein associations compared to the sublethal contrast, and was composed by *caspase-8*, *caspase-9*, *bax*, *birc2* (inhibitor of apoptosis protein-like), *ciapin1* (cytokine induced apoptosis inhibitor 1), *isg20* (apoptosis-enhancing nuclease-like), *ccar1* (cell division cycle and apoptosis regulator 1), *pawr* (pro-apoptotic WT1 regulator) and *PERP* (p53 apoptosis effector related to PMP22). Among these, BAX promotes activation of caspase-3, and thereby apoptosis (Gavathiotis
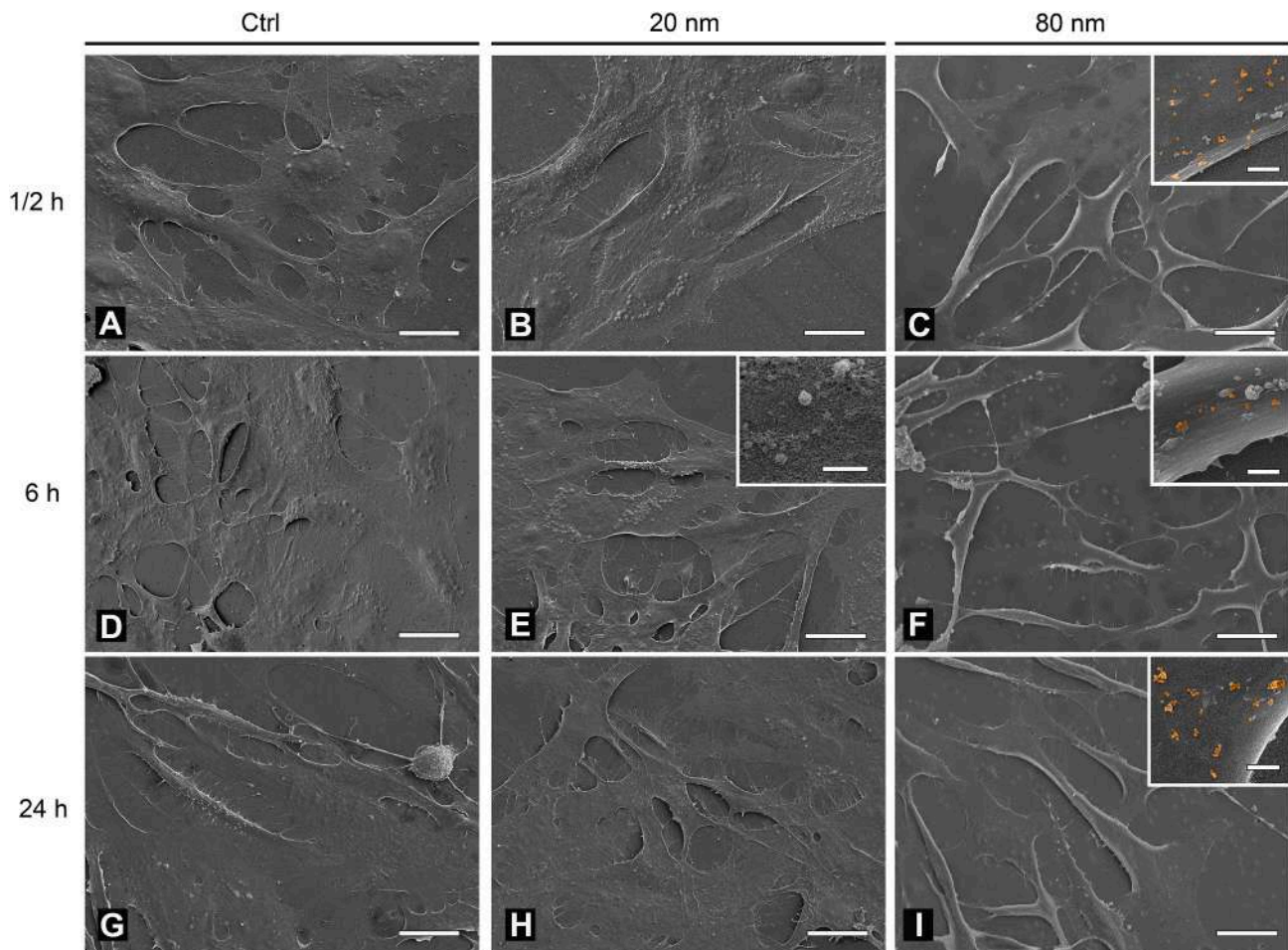
Fig. 7. SEM micrographs of RTG-2 cells along exposure times. Untreated cells (Ctrl) are shown in A, D and G; 20 nm PS-NPs-treated cells are shown in B, E and H; 80 nm particles-treated cells are shown in C, F and I. Scale bars A–I = 20 μm, insets = 1 μm.

et al., 2008), while PERP and CCAR1, both downregulated in treated SAF-1, are involved in cell-cell junction, epithelial integrity and the positive regulation of cell proliferation.

Cyclin-dependent serine/threonine kinases (CDKs) and their regulatory subunits, cyclins, both key regulators of cell cycle (Herwig and Strauss, 1997), were differentially impacted by the two PS-NPs doses. While the sublethal contrast only resulted in the downregulation of *ccnb1* (cyclin B1), the lethal dose caused a downregulation of several cyclin-related transcripts, with $\log_2$ FCs and p-adj as low as -5.89 and 2.30E-135. These were, for instance, *proca1* (protein interacting with cyclin A1), *cdk16* (cyclin-dependent kinase 16-like), *ccne2* (G1/S-specific cyclin-E2-like), *ccnb3* (G2/mitotic-specific cyclin-B3-like), *ccna2* (cyclin A2), *nucks1a* (nuclear casein kinase and cyclin dependent kinase substrate 1), *cdk6* (cyclin dependent kinase 6), *ccnb1* (cyclin B1), *cks2* (cyclin-dependent kinases regulatory subunit 1-like), *cdk1* (cyclin dependent kinase 1), *ccnd2b* (G1/S-specific cyclin-D2-like) and *cables1* (Cdk5 and Abl enzyme substrate 1). Only the lethal PS-NPs dose negatively impacted *egfra* (epidermal growth factor receptor), *vegfab* (vascular endothelial growth factor A-A-like), *vegfc* (vascular endothelial growth factor C), *areg* (proheparin-binding EGF-like growth factor) and *EFEMP1* (EGF containing fibulin extracellular matrix protein 1). On the other hand, only the lethal dose promoted the expression of *cdkn1a cyclin-dependent kinase inhibitor 1-like*, encoding for a potent inhibitor of cyclin-CDK2 or -CDK4 complexes, and thus regulating cell cycle progression at G1.

All transcriptome functional analyses made use of *D. rerio* ENTREZ gene IDs.

The over-representation analysis on GO terms conducted for the sublethal contrast revealed 5 (i.e. ribonucleoprotein complex biogenesis, transmembrane transport, intra-Golgi vesicle-mediated transport, translational initiation and ribosome biogenesis) and 74 (e.g. actin cytoskeleton organization, actin filament-based process, cytoskeleton organization, cell adhesion and regulation of cell morphogenesis) over-represented biological processes within the up- and down-regulated sets of DEGs, respectively. The over-represented molecular functions were mostly related to translational regulation (up-regulated DEGs) and binding of cytoskeletal protein, DNA for transcription factor activity and cell adhesion molecule (down-regulated DEGs) (Table S3A–B). A more profound response to the lethal PS-NPs dose was highlighted: 28 (e.g. protein localization to endoplasmic reticulum, translation, peptide biosynthetic process, peptide metabolic process, response to endoplasmic reticulum stress and autophagy) and 158 (e.g. mitotic cell cycle, chromosome organization and segregation, steroid biosynthetic process, ATP biosynthetic process, chemotaxis, cell adhesion, DNA recombination and repair, actin filament polymerization, cellular respiration, cytoskeleton organization and cellular response to DNA damage stimulus) biological processes were over-represented within the up- and down-regulated sets of DEGs, respectively (Table S3C–D).

The GSE analysis identified 9 and 5 enriched KEGG pathways from the sublethal and lethal contrasts (Table S4A–B, Fig. 10A–B). With regard to the former, a negative normalized enrichment score (NES) (i.e. associated with the control group, and therefore negatively impacted by PS-NPs) was found for 7 out of 9 gene sets, namely "ECM-receptor interaction", "TGF-beta signaling pathway", "Focal adhesion",
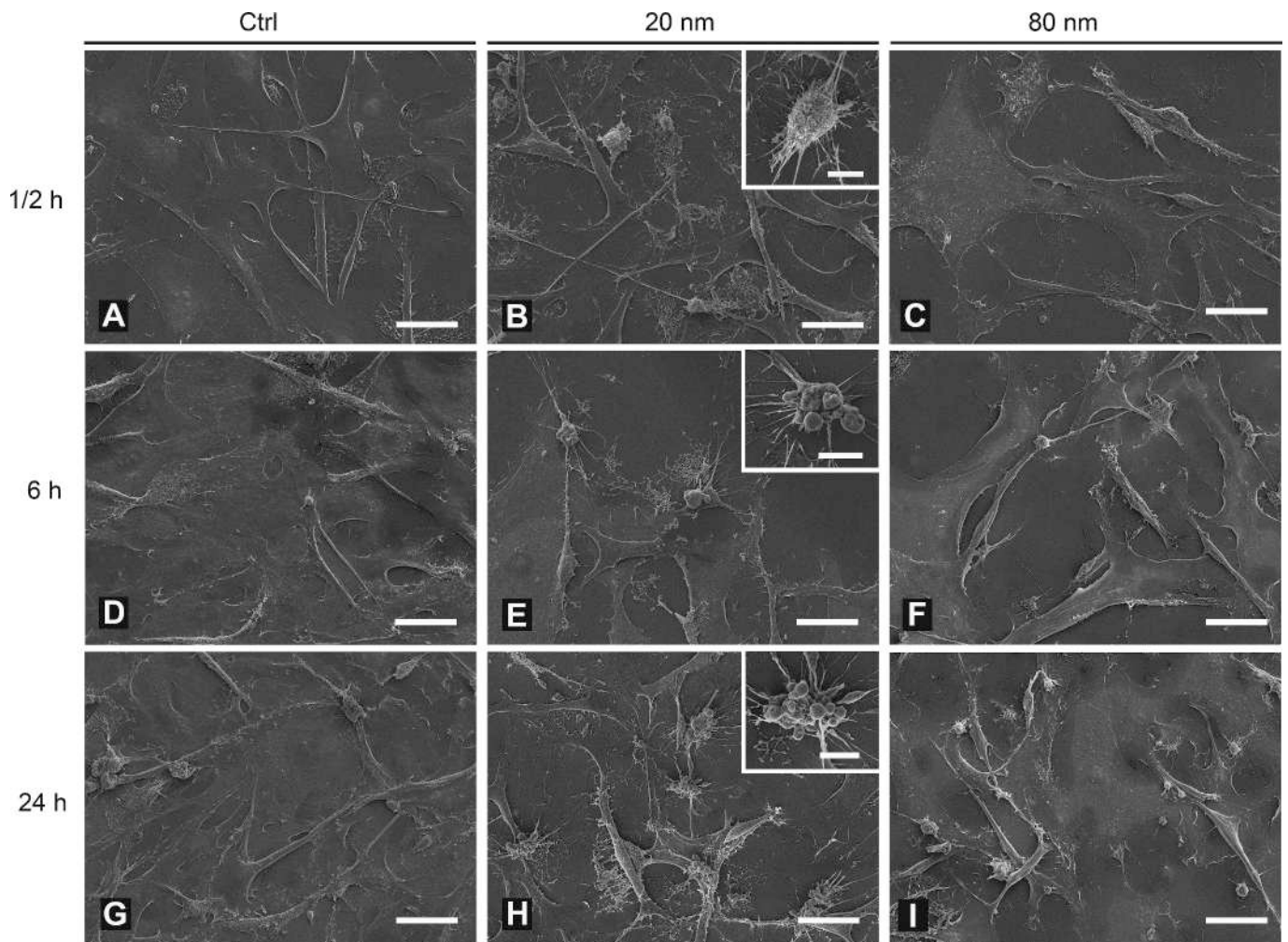
Fig. 8. SEM micrographs of SAF-1 cells along exposure times. Untreated cells (Ctrl) are shown in A, D and G; 20 nm PS-NPs-treated cells are shown in B, E and H, and corresponding insets; 80 nm particles-treated cells are shown in C, F and I. Scale bars A–I = 20 μm, insets = 5 μm.

"Regulation of actin cytoskeleton", "Steroid biosynthesis", "Adherens junction" and "Tight junction", sorted ascendingly. In the ECM-receptor interaction pathway, most of the extracellular matrix (ECM)- and integrin-encoding genes had a negative log$_2$ FC (Fig. S1A). In the "Steroid biosynthesis" pathway, *tm7sf2* (Transmembrane 7 superfamily member 2), *lss* (lanosterol synthase), *ebp* (EBP cholestenol delta-isomerase), *nsdhl* (NAD(P) dependent steroid dehydrogenase-like), *dhcr7* (7-dehydrocholesterol reductase), *msmo1* (methylsterol mono-oxygenase 1), *fdft1* (farnesyl-diphosphate farnesyltransferase 1) and *sqlea* (squalene epoxidase a), which all mediate the cascade enzymatic reactions leading to cholesterol synthesis, were identified as core enrichment genes (Table S4A). A positive NES was instead obtained for the "Aminoacyl-tRNA biosynthesis" and "Ribosome biogenesis in eukaryotes" gene sets. In general, SAF-1 treated with the sublethal PS-NPs dose underperformed in terms of maintenance of cell morphogenesis, hormone synthesis and response to microenvironmental conditions, but likely attempted to overcome the stressful condition by positively regulating protein biosynthesis and assembly.

The GSEA conducted on the lethal contrast results revealed that the highest PS-NPs dose negatively impacted 4 out of the 5 significantly enriched gene sets, namely "Carbon metabolism", "Steroid biosynthesis", "TGF-beta signaling pathway" and "Focal adhesion". "Protein processing in endoplasmic reticulum", on the other hand, was stimulated (Table S4B, Fig. 10B). "Focal adhesion", "TGF-beta signaling pathway" and "Steroid biosynthesis" appeared as significantly and negatively enriched by both the sublethal and lethal PS-NPs doses.

An estimate of the actual impact of transcriptional changes caused by the two PS-NPs doses was obtained with a SPI analysis by combining both overrepresentation (p NDE) and perturbation (p PERT) data. The sublethal PS-NPs dose led to the significant inhibition of the "Focal adhesion" (ID: 4510) and "Regulation of actin cytoskeleton" (ID: 4810) KEGG pathways. These also resulted as significantly inhibited (at Bonferroni and FDR correction, respectively) by the lethal dose, together with "ECM-receptor interaction" (ID: 4512). "Protein processing in endoplasmic reticulum" (ID: 4141) was instead activated by the PS-NPs treatment at the lethal dose (Fig. 10C). The complete test results, along with KEGG links of annotated pathways, are available in Table S5A–B.

3.5.2. The transcriptional induction of programmed cell death was validated by Annexin V/Propidium iodide and DNA fragmentation

To validate the cell death mechanism put in place by SAF-1 in response to PS-NPs exposure, a flow cytometric apoptosis-necrosis assay based on Annexin V/PI double staining was quantified at 24 hpi at the lethal dose as per cytotoxicity screening.

Cells displayed clear apoptotic signatures, with rate percentages of 12.2 % and 23.3 % for early and late apoptosis, respectively, compared to necrotic and viability evidence in 5.7 % and 58.9 % of events (Fig. 11AC). The above features appeared with rates of 3.1 %, 1.5 %, 1.7 % and 93.6 % (negative control, Fig. 11AA) and in 23.9 %, 36.4 %, 2.2 % and 37.5 % (positive control, Fig. 11AB).

DNA fragmentation in PS-NPs-treated cells was visualized by a TUNEL assay. The first occurrence of the strong nuclear green
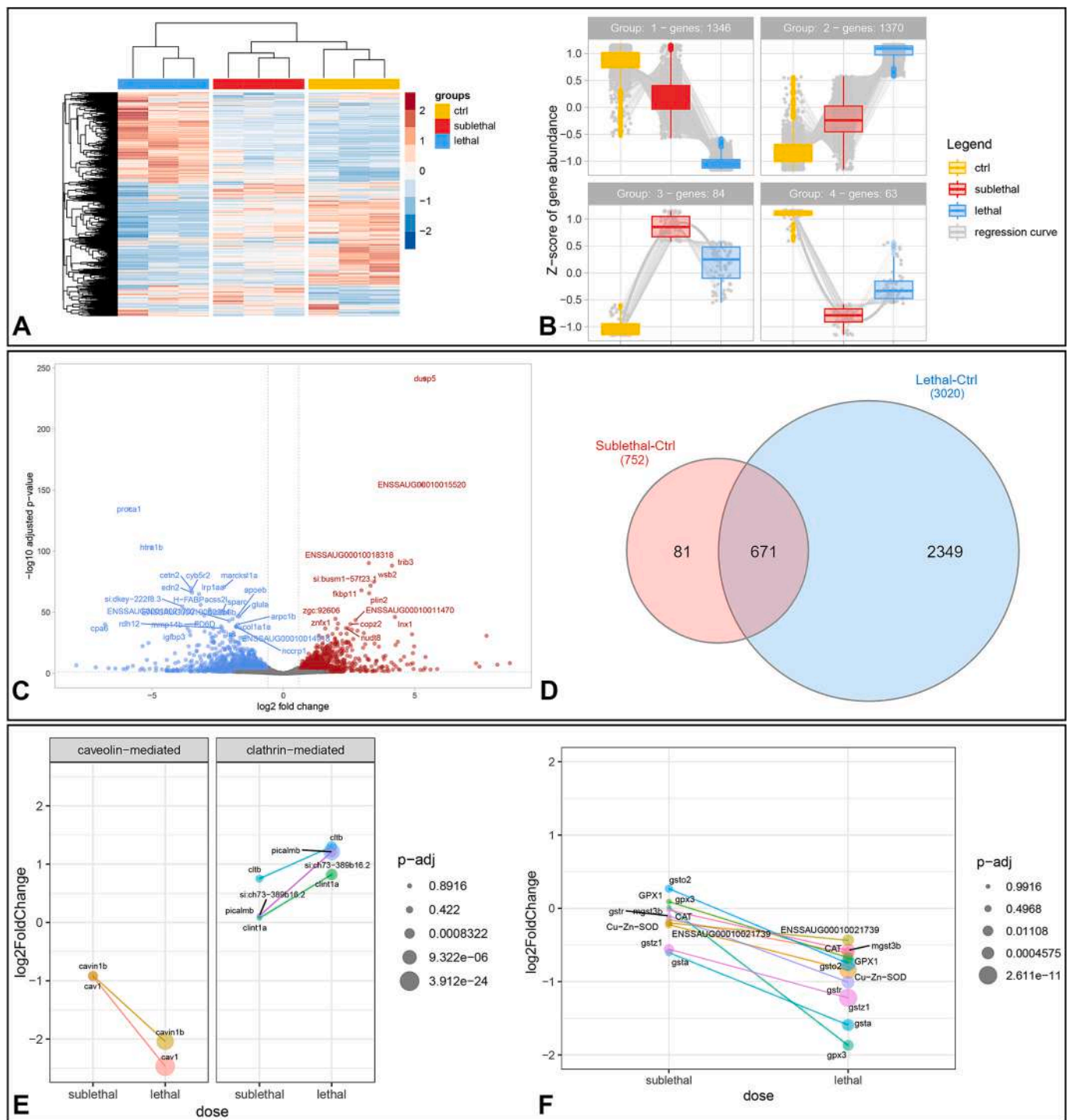
Fig. 9. A) Heatmap and hierarchical clustering of Z-score-transformed normalized counts of the 4000 genes associated with the greatest among−treatment variance. B) Four-group clustering of Z-score-transformed gene expression resulting from the Likelihood Ratio Test investigating the goodness of fit of a reduced model in DESeq2. Boxplots report expression patterns across experimental groups. C) Volcano plot ($\log_{10}$ transformed adjusted *p*-values over shrunk $\log_2$ fold change) of all genes tested for differential expression within the lethal contrast. Blue (down-regulation) and red (up-regulation) coloring applied when adjusted p-value and absolute value of $\log_2$ fold change were lower than 0.05 and >0.58 (i.e. fold change = 1.5), respectively. The 40 genes whose DE status was supported by strongest statistics (i.e. lowest adjusted p-value) were labeled by ZFIN gene name or Ensembl gene ID (if gene name was not available). D) Area-proportional Venn diagram showing the unique and overlapping DE genes between the sublethal and lethal contrasts. E) Expression patterns ($\log_2$ FC estimates relative to controls) of selected color-coded genes involved in caveolin- and clathrin-mediated endocytic pathways along PS-NPs doses. Statistical support of the transcriptional pattern (i.e. BH-adjusted p-value) is represented by point size. Gene labels as per NCBI or ZFIN gene names. *cav1*: ENSSAUG00010009010; *cavin1b*: ENSSAUG00010009474; *clint1a*: ENSSAUG00010027473; *cltb*: ENSSAUG00010007896; *picalmb*: ENSSAUG00010019361; si:ch73-389b16.2: ENSSAUG00010009118. F) Expression patterns ($\log_2$ FC estimates relative to controls) of selected color-coded genes encoding for antioxidant enzymes along NP doses. Statistical support of the transcriptional pattern (i.e. BH-adjusted p-value) is represented by point size. Gene labels as per NCBI or ZFIN gene names. *CAT*: ENSSAUG00010005803; *Cu-Zn-SOD*: ENSSAUG00010014144; *glutathione peroxidase 1a*: ENSSAUG00010021739; *GPX1*: ENSSAUG00010007839; *gpx3*: ENSSAUG00010003792; *gsta*: ENSSAUG00010003915; *gsto2*: ENSSAUG00010015523; *gstr*: ENSSAUG00010003870: *gstz1*: ENSSAUG00010005093; *mgst3b*: ENSSAUG00010015792.
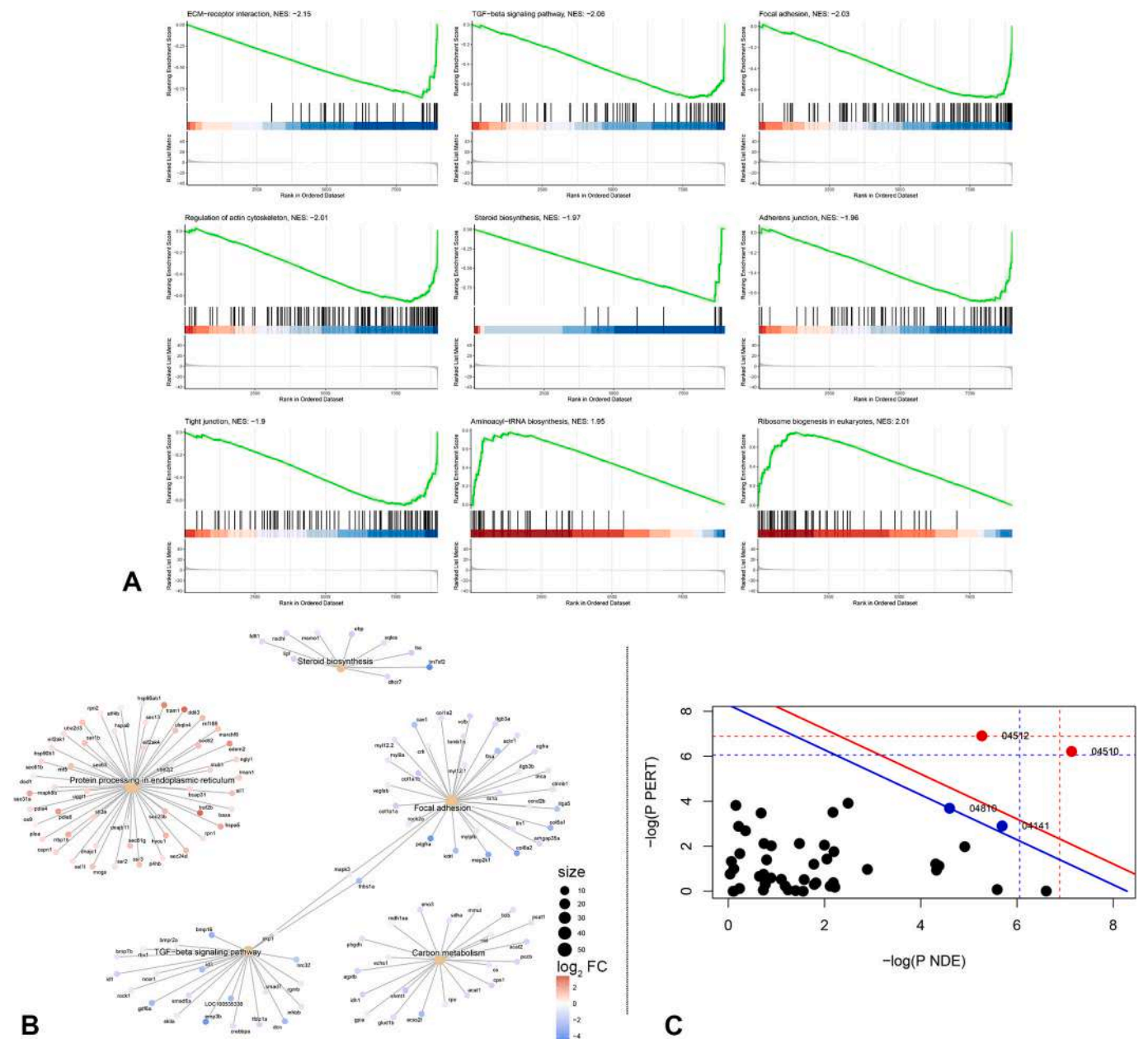
Fig. 10. A) Statistically enriched KEGG pathways modulated by the sublethal PS-NPs dose. The normalized enrichment score (NES) is reported next to the pathway title. The top, middle and bottom panels of the plots depict the profile of the running enrichment score, the position of gene set members in the rank-ordered list, and the value and distribution of the ranking metric, respectively. B) Log_2 FC-annotated gene-category network plot of core enrichment genes within the lethal contrast. Dot size of categories is proportional to the number of genes. C) Two-way SPIA evidence plot illustrating the relationship between pathway perturbation (P PERT) and over-representation (P NDE). Each KEGG pathway tested is represented by a dot: ID: 4510: "Focal adhesion"; ID:4810: "Regulation of actin cytoskeleton"; ID:4512: "ECM-receptor interaction"; ID:4141: "Protein processing in endoplasmic reticulum".

fluorescence coinciding with the DAPI staining was seen at 3 hpi (Fig. 11B). Negative controls lacked any green fluorescence.

3.5.3. PS-NPs-induced cell death was ROS-independent

The overall redox state of cells induced by PS-NPs was investigated with a DCFDA assay. Exposure to 20 nm PS-NPs at lethal dose did not result in any significant increase in ROS production compared to the negative controls at 3 and 24 hpi (Fig. 12). The hydrogen peroxide and the medium controls did not statistically differ from the negative control, while a marked increase in fluorescence (i.e. 39.5- and 19.3-fold higher compared to the negative control at 3 and 24 hpi) was recorded for the positive control, as expected.

4. Discussion

The integration of *in vitro* models into nanoparticle research has become indispensable for understanding their impact on living organisms. This *in vitro* approach not only enhances the reliability of toxicological evaluations but also aligns with ethical imperatives to minimize animal use in research (Almeida et al., 2019), in line with the 3Rs principle advocated by the EU (Moné et al., 2020; Revel et al., 2021). Fish cell lines have emerged as transformative tools, allowing for comprehensive hazard characterization beyond traditional *in vivo* models (Katsumiti and Cajaraville, 2019; Langner et al., 2011; Rafael et al., 2010; Villalba et al., 2017; Ye et al., 2006). They provide unparalleled opportunities to dissect the molecular-level effects of emerging
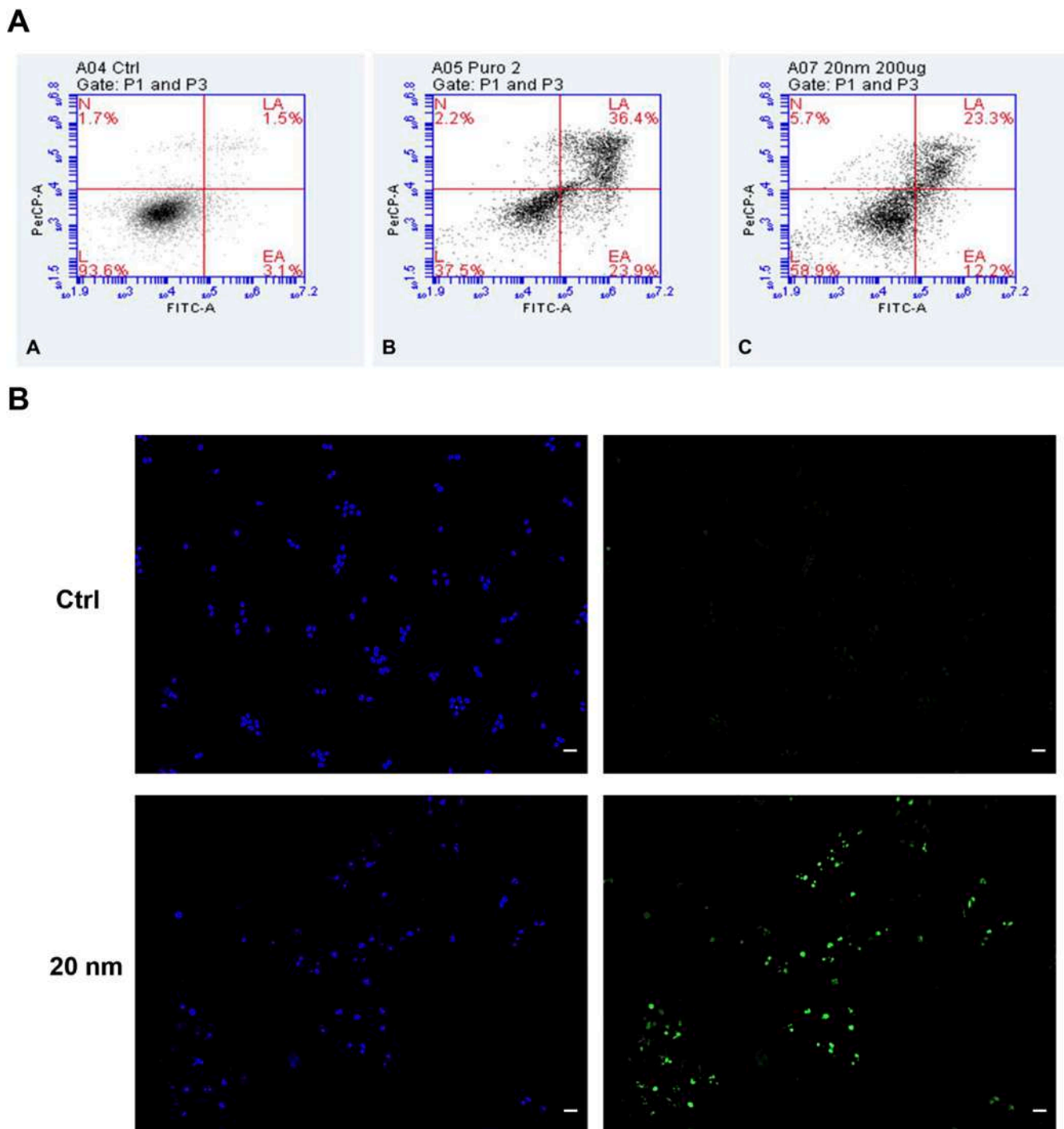
Fig. 11. A) Flow cytometric Annexin V/Propidium Iodide staining assay of SAF-1, with negative control (A), positive control (B) and 20 nm PS-NPs-treated cells (C). Percentages at each quadrant corner indicate positivity of viable (L), early/late apoptotic (EA/LA) or necrotic (N) cells. Propidium iodide and Annexin V positivity were quantified by PerCP (Peridinin-Chlorophyll-Protein) and FITC (Fluorescein isothiocyanate) fluorescence channels. B) TUNEL assay PS-NPs-treated SAF-1. Cells were incubated with the lethal dose of 20 nm PS-NPs. DAPI-stained nuclei of treated SAF-1 show a strong green fluorescence signal (TUNEL-positive) with respect to controls (Ctrl). Scale bars = 20 μm.

contaminants (Goswami et al., 2022; Morcillo et al., 2017; Pannetier et al., 2018; Vo et al., 2014), and some are recognized as good biological models for marine and freshwater ecotoxicology studies related to NPs (e.g. Barreto et al., 2018; Caminada et al., 2006).

In this study, we evaluated the ecotoxicological effects induced by 20 and 80 nm PS-NPs on RTG-2 and SAF-1 cell lines, both exhibiting fibroblast-like morphology. These cell lines are scientifically recognized *in vitro* piscine models for assessing physiological responses to emerging contaminants (Bermejo-Nogales et al., 2017; Fent, 2001; Goswami et al., 2022; Hernández-Moreno et al., 2022; Ruiz et al., 2020). Employing a step-wise approach towards increasing biological relevance and leveraging omics data, as per best practices recommended by the OECD Series on Testing and Assessment (No. 171 and 334), mechanistic information eventually unraveled the mode of action underlying the detrimental effects of PS-NPs.

PS-NPs were characterized in terms of shape, size, PDI and
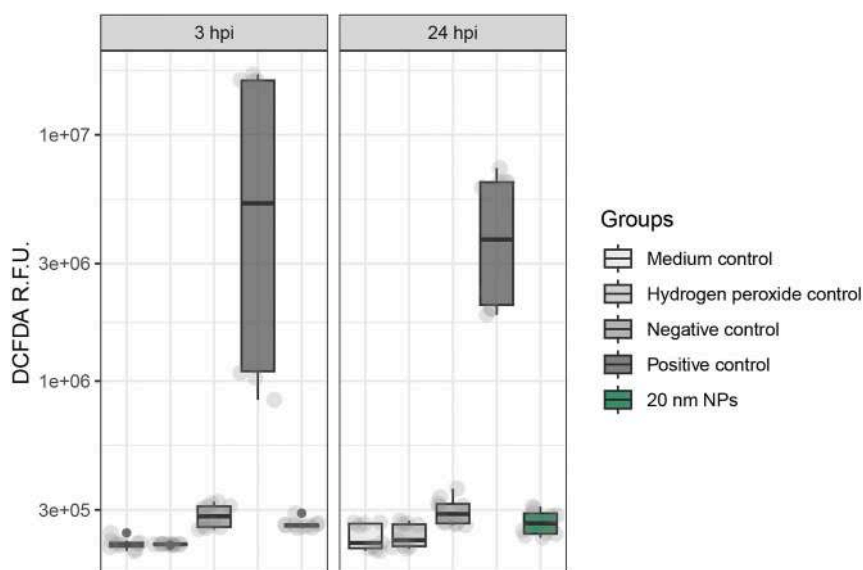
Fig. 12. ROS quantification with 2′,7′-dichlorodihydrofluorescein diacetate following 3- and 24-h exposure to 200 μg/mL of 20 PS-NPs, together with negative, positive and internal controls.

ζ-potential. TEM analysis following the negative staining confirmed their size and round shape according to the manufacturer's certificate of analysis. Their tendency to form aggregates was also evidenced. DLS measurements in water and culture medium, either supplemented with 10 and 30 % FBS or not, revealed an increase in size associated with a decrease in absolute value of ζ-potential, in line with (Almeida et al., 2019; Kihara et al., 2021; Revel et al., 2021; Sendra et al., 2021). We point to the fact that the ζ-potential was influenced by the cell culture media itself rather than the percentages of FBS supplementation, therefore allowing for direct comparisons of the obtained results. FBS supplementation instead affected the D_h of PS-NPs (Table 1), likely due to aggregation and the protein corona paradigm (Kihara et al., 2021; Liu et al., 2021), which involves the transient surface adsorption of proteins, ions, and lipids when nanomaterials are exposed to biological fluids, also visually observed by ultrastructural analyses (Figs. 4–5, 7–8) (Cedervall et al., 2007; Walkey and Chan, 2012).

The highest tested dose of 20 nm PS-NPs proved lethal to SAF-1 cells in a time-dependent manner from 6 hpi onwards. Opposite responses were seen in RTG-2 cells, which exhibited cytotoxicity only at 800 μg/mL. Results from such viability assays were modeled by nonlinear regression for data extrapolation and comparison purposes across cell models and species (Franco and Lavado, 2019): the LC50 parameter underscored the heightened sensitivity of SAF-1 to the smallest PS-NPs size (i.e. approximately 4-fold higher than RTG-2). Notably, these doses fall within the concentration range reported for plastic NPs collected globally, i.e. 0.3–488 μg/mL (Shi et al., 2024), and align to recent literature of the field (e.g. Brandts et al., 2023; He et al., 2020; Jeong et al., 2018; Magni et al., 2018; Sendra et al., 2020, 2021; Yang and Wang, 2023; Zhou et al., 2023). On the other hand, 80 nm PS-NPs i) generally enhanced cell viability uniquely in RTG-2 up to 400 μg/mL (0.5 hpi) or 100 μg/mL (6 and 24 hpi), with cells exposed to 800 μg/mL not suffering cytotoxicity even at 24 hpi; ii) did not positively impact viability of SAF-1, and caused only a slight decrease in ATP contents with 100 μg/mL (24 hpi) and 200 μg/mL (0.5 and 24 hpi) and iii) were much less cytotoxic than the 20 nm ones, as an LC50 could not be reliably calculated.

The viability data emphasize the importance of NPs size in dictating cellular responses. NPs are cytotoxic agents (e.g. Guimarães et al., 2021; Revel et al., 2021), with intrinsic features such as polymer, size, shape, dose and surface charge determining their harmful effects (e.g. Augustine et al., 2020; Li et al., 2019; Roshanzadeh et al., 2020; Sun et al.,

2020). Size-dependency of cell viability impacts, or more generally cellular effects, was highlighted recently for both NPs and microplastics (Nardi et al., 2024; Pannetier et al., 2020). Smaller particles are generally more toxic than larger ones of the same composition (Katsumiti and Cajaraville, 2019): below the threshold of 30 nm in size, NPs exhibit excess surface energy and enhanced reactivity and thermodynamic instability due to increased ratio of surface area to total atoms (Auffan et al., 2009). Smaller-sized NPs may also be able to penetrate membranes more easily (Guerrera et al., 2021; Johnston et al., 2010; Liu et al., 2021).

The stimulation of cell viability, which we often observed in RTG-2 at sublethal doses and exposure times, is confirmed by recent literature (Forte et al., 2016; Hesler et al., 2019; Poma et al., 2019; Xu et al., 2019) and may be due the priming of stress-related cellular metabolic responses (Ali et al., 2024; Forte et al., 2016; Poma et al., 2019) leading to an increase of intracellular ATP levels. Enhanced viability was also seen following the exposure to larger NPs (e.g. 100 nm, Forte et al., 2016) or complexation with carbohydrates, proteins and lipids (Li et al., 2023). The latter research also highlighted the variation in PS-NPs protein corona composition depending on the interacting food matrices. The peculiar RTG-2 response to PS-NPs compared to SAF-1 may be explained by differences in the protein corona absorption patterns, which modifies the biological identity of nanomaterials (Zhang et al., 2020) and contribute to determining their actual toxicity and fate (Drasler et al., 2017; Lesniak et al., 2010; Walkey et al., 2014).

Cell uptake is influenced by ζ-potential, shape and hydrophobicity/ hydrophilicity of nanomaterials (Kevadiya et al., 2019). Despite the preference for positively charged NPs for cellular uptake due to favorable positive-negative electrostatic interactions, both sizes of PS-NPs engaged and adhered with cell membranes of RTG-2 and SAF-1 cells already by 0.5 hpi (Figs. 4–8). The simultaneous exposure assayed at the confocal microscopy could help researchers better understand their potential hazards, as environmental NPs occur as heterogeneous mixture (Khan and Jia, 2023), but a worsening of the cytotoxic effect was not detected (data not shown). Following membrane penetration, NPs interact with cytoplasmic proteins, nucleus, and other cellular organelles (Augustine et al., 2020): in our case, 20 nm PS-NPs were rapidly endocytosed and vesicle-translocated to the perinuclear area and within the nucleus (Domenech et al., 2021), damaging the nuclear envelope of both cell models; those of 80 nm were in addition shown to associate to and enter lysosomal membrane (Liu et al., 2021) and phagocytic

vesicles. Our transcriptional data assisted in elucidating the endocytic pathway of 20 nm PS-NPs. Genes encoding for caveolin- and clathrin-mediated endocytic pathways underwent an opposite transcriptional regulation, and PS-NPs dosage influenced the statistical support of these findings (Fig. 9E). It is assumed that lowering cholesterol would increase cholesterol-independent clathrin-mediated endocytosis (Khan and Jia, 2023): indeed, the "Steroid biosynthesis" gene set was negatively enriched at both doses and the core enrichment genes were sequentially involved in the enzymatic reactions leading to cholesterol synthesis. Research conducted in vitro confirmed latex beads and PS particles smaller than 200 nm to mainly undergo clathrin-mediated endocytosis (Fazlollahi et al., 2011; Ji et al., 2021; Rejman et al., 2004), even though macropinocytosis, usually involved in the endocytosis of larger particles (Li et al., 2019), may also be suitable for particles within the 200 nm size boundary (Guarnieri et al., 2011; Reinholz et al., 2018). This is an actin-driven pathway (Mylvaganam et al., 2021), but the "Regulation of actin cytoskeleton" gene set was negatively impacted as per GSE and SPI analyses, respectively (Tables S4A, S5B). Altogether, these data support the assumption that 20 nm PS-NPs are endocytosed via a clathrin-mediated pathway.

The impact of PS-NPs on cell morphology and ultrastructure was also size-dependent: at the lethal dose determined by viability assays, only the smallest ones induced clear apoptotic signatures on SAF-1. A similar blebbing morphology and activation of apoptotic signaling was previously observed only in human alveolar cells exposed to PS-NPs (Roshanzadeh et al., 2020; Ruenraroengsak and Tetley, 2015).

RNA sequencing was exploited to deepen the understanding of the functional response of SAF-1 cells exposed to 20 nm PS-NPs. Multidimensional transcriptomics data evidenced the more severe impacts of the lethal than the sublethal PS-NPs dose compared to control cells. The greater sensitivity of such an approach evidenced how SAF-1 exposed to the sublethal dose, despite not suffering any cytotoxicity, promoted ribosome biogenesis and translation, likely in an attempt to overcome the PS-NPs-imposed stress (Khan and Jia, 2023). The selective over-expression of ribosome-related genes is part of the so-called environmental stress response (ESR) enacted by eukaryotic cells exposed to a variety of stresses (Gasch et al., 2000). Activation of the ESR was found to promote cell survival in stressful conditions and to correlate with increased resistance to stress (Terhorst et al., 2023 and references therein).

Polystyrene plastics were previously reported to induce apoptosis *in vitro* through PI3K/AKT and Bcl-2/Bax pathways in a human epithelial cell model (e.g. Qin et al., 2022) and *in vivo* via ROS-mediated p53 signaling pathway following a 35-day in zebrafish (e.g. Umamaheswari et al., 2021). The major PS-NPs impacts on SAF-1 were herein found to be the massive inhibition of genes and pathways related to ECM organization, tight junctions, focal adhesion, protein processing in endoplasmic reticulum, mitochondria and the cell cycle. Some were affected by both doses (Fig. 10A–C), but in all cases, these are well-established ROS-independent apoptotic triggers encompassed within both the extrinsic and intrinsic pathways. Similar changes in molecular signaling pathways were observed following *in vivo* exposure of Tilapia larvae to PS-NPs (Pang et al., 2021) and, partially, after prolonged *in vitro* exposure of to murine primary skin cell cultures including dermal fibroblasts and epidermal keratinocytes to PS nano- and microplastic in the 0.2–6 μm size range (Schmidt et al., 2023). The DCFDA assay, which did not detect any increase in ROS, provided validation of such a condition (Fig. 12). Nevertheless, the lethal dose elicited a marked downregulation of 10 genes encoding for antioxidant enzymes (Fig. 9F), possibly leading to a disruption of the redox homeostasis (He et al., 2017).

Both the cell-cell and cell-matrix adhesion drive the commitment to either cell survival or apoptosis. Cell adhesion to the ECM is mediated by integrins, which are glycoproteins demonstrated to trigger many signaling pathways regulating actin cytoskeleton architecture, cell motility and proliferation, in addition to assisting cells in avoiding apoptosis (Ruoslahti and Reed, 1994). Our data report a significant and

strong dose-dependent downregulation in the expression of the integrin network including *itgb1b* (integrin beta-1-like), *itgb2* (integrin beta-2-like), *itgb3a* (integrin beta-3-like), *itgb3b* (integrin subunit beta 3), *itgb4* (integrin, beta 4), *itga5* (integrin alpha-5-like), *ILK* (integrin-linked protein kinase-like), *ctnna1* (catenin alpha 1), *ctnnb1* (catenin beta 1) and ENSSAUG00010024274 (catenin beta-1-like). When integrin activity is inhibited, epithelial cells lose cell-cell adhesion and undergo apoptosis (Ruoslahti and Reed, 1994); integrin dysfunction and the lack of integrin interaction with ECM results in epithelial cell death by detachment, the so-called anoikis, and loss of integrin-mediated cell-matrix contact is an established apoptosis-inducer (Frisch and Ruoslahti, 1997); ECM regulates apoptosis in mammary epithelial cells through an integrin-dependent negative regulation of interleukin-1 beta converting enzyme expression (Boudreau et al., 1995). The sites where integrins attach to the matrix, form structural connections with the cytoskeleton and facilitate signal transmission are known as focal adhesions. An inhibition of the "Focal adhesion" and "Regulation of actin cytoskeleton" gene sets was observed in cells lethally treated with PS-NPs (Table S4B). Focal adhesions include structural components such as actin as well as protein tyrosine kinase like FAK (Focal Adhesion Kinase). FAK is a tyrosine kinase that associates temporally and spatially with, and whose activation is dependent upon clustering to, integrins (Otey, 1996; Pelletier et al., 1995). While FAK activation and maintenance via integrin engagement is critical for suppressing apoptosis (Crouch et al., 1996; Hungerford et al., 1996), its caspase-mediated cleavage, which may occur with different sensitivities depending on the caspase molecule involved (Wen et al., 1997), represents an irreversible commitment to programmed cell death (Gervais et al., 1998). We could annotate FAK via blastx (gene ID ENSSAUG00010003078) but no expression data was available (Table S2D).

"TGF-beta signaling pathway" was also inhibited by the lethal PS-NPs dose. TGFβ regulates essential cellular functions such as cellular proliferation, differentiation and apoptosis, and its signaling induces a chronic overload of ECM proteins to the endoplasmic reticulum (ER) (Okumura et al., 2017). Conformational changes of secondary structures are among the possible outcome following NPs exposure of proteins (Gopinath et al., 2019), and molecular dynamics provided *in silico* evidence of protein misfolding due to secondary structure modifications when simulating interactions with NPs of various chemistries (Hollóczki and Gehrke, 2019). In this work, only SAF-1 treated with the lethal PS-NPs dose activated the "Protein processing in endoplasmic reticulum" pathway, likely in an initial attempt to restore a correct folding and, later, to degrade terminally-misfolded proteins via the unfolded protein response (UPR). We observed a general upregulation in the expression of genes involved in all steps of ER processing of misfolded proteins, such as protein recognition by luminal chaperones (*hyou1*, *hspa5*, *hsp90b1* and several genes encoding for the DnaJ heat shock protein family Hsp40), ER stress and activation of the UPR signaling pathway caused by the accumulation of misfolded proteins (i.e. *eif2ak1*, genes encoding for several cyclic AMP-dependent transcription factors and *ddit3*), protein targeting, ubiquitination and translocation for ER-associated proteasomal degradation (ERAD) (i.e. *edem2*, *pdia4* and *pdia6*, *ssr2* and *ssr3*, *bcap31*, *tram1*, *marchf6*, *sel1l*, *rnf5*, *ube2d3*, *ubqln4*, and *rbx1*). We point out that a prolonged activation of the UPR pathway and the resulting condition of ER stress are recognized apoptotic cell death initiators via the up-regulation of the C/EBP homologous protein (CHOP), encoded by *ddit3*, and its upstream regulatory pathway (Ariyasu et al., 2017; Hu et al., 2019) (Fig. S1B).

Mitochondrial perturbation was suggested by the upregulated expression of *bax*, which determines cytochrome *c* release (Peña-Blanco and García-Sáez, 2018), and of *caspase-9*, recruited and activated by the Apaf-1-cytochrome *c* apoptosome, leading to activation of effector caspases, cytoplasmic endonuclease activation, nuclear disruption, cytoskeletal protein proteolysis and cell death (Han et al., 2023). Importantly, the energy required for apoptosome assembly is supplied by dATP hydrolysis (Kim et al., 2005), which may further explain the

cell viability results obtained.

In addition to the above, cell viability is largely dependent upon cell cycle regulation. The cell cycle is an intricate sequence of events that requires precise regulation for a cell to proliferate, differentiate, or undergo apoptosis. The progression from G1 (growth phase 1) to the S (DNA synthesis) phases is influenced by numerous growth factors, with the two main check-points being in the late G1 phase, especially important for the onset of apoptosis, and immediately prior to entry into the M phase (Evan et al., 1995). The epidermal growth factor (EGF) has mitogenic activity and is majorly involved in growth of a wide variety of epithelial cell types and fibroblasts (Santini et al., 2000). The massive downregulation of G1-related CDKs and their regulatory subunits as well as of growth factors and corresponding receptors, all impacted with different dose-dependent extents, was predominant in our data, and likely contributed to directing the cell towards a cell death program. Cleavage of chromosomal DNA and translocation of phosphatidylserine to the outer leaflet of the cell membrane, together with blebbing and cell shrinkage described above (Fig. 8), are hallmarks of apoptosis. Evidence of DNA fragmentation, markedly observed following 3 hpi with to the 20 nm-PS-NPs lethal dose, as well as of early and late apoptotic events, overall induced in 35.5 % of treated cells at 24 hpi, was validated via TUNEL and Annexin V/PI assays, respectively (Fig. 11A–B).

5. Conclusions

This study fully exploited recognized *in vitro* teleost cell lines and revealed dose-, size- and model-dependent differences in harmful impacts of PS-NPs. Smaller PS-NPs (20 nm) caused profound cytotoxicity in fish cell lines, triggering apoptosis and disrupting critical molecular pathways such as cell-cell/matrix adhesion, regulation of actin cytoskeleton and protein processing, while not imposing any oxidative stress within the assessed timeframe. The ecotoxicological hazard to aquatic organisms was highlighted, emphasizing the need for further investigation into their long-term effects and mitigation strategies.

Supplementary data to this article can be found online at https://doi.org/10.1016/j.scitotenv.2024.173159.

CRediT authorship contribution statement

P.R. Saraceni: Writing – original draft, Validation, Investigation, Funding acquisition, Formal analysis. **A. Miccoli:** Writing – original draft, Visualization, Software, Project administration, Funding acquisition, Formal analysis, Data curation. **A. Bada:** Writing – review & editing, Investigation. **A.R. Taddei:** Writing – review & editing, Investigation. **M. Mazzonna:** Writing – review & editing, Investigation. **A.M. Fausto:** Writing – review & editing. **G. Scapigliati:** Writing – review & editing, Resources. **S. Picchietti:** Writing – review & editing, Writing – original draft, Supervision, Project administration, Conceptualization.

Declaration of competing interest

The authors declare no competing financial interests or personal relationships that could have appeared to influence the work reported in this paper.

Data availability

Experimental data will be made available on request. RNAseq raw data were deposited into the NCBI SRA database under the BioProject ID PRJNA1041099.

References

Ali, N., Katsouli, J., Marczylo, E.L., Gant, T.W., Wright, S., Bernardino de la Serna, J., 2024. The potential impacts of micro-and-nano plastics on various organ systems in humans. eBioMedicine 99, 104901. https://doi.org/10.1016/J.EBIOM.2023.104901.

Almeida, M., Martins, M.A., Soares, A.M.V., Cuesta, A., Oliveira, M., 2019. Polystyrene nanoplastics alter the cytotoxicity of human pharmaceuticals on marine fish cell lines. Environ. Toxicol. Pharmacol. 69, 57–65. https://doi.org/10.1016/j.etap.2019.03.019.

Ariyasu, D., Yoshida, H., Hasegawa, Y., 2017. Endoplasmic reticulum (ER) stress and endocrine disorders. Int. J. Mol. Sci. 18, 382. https://doi.org/10.3390/ijms18020382.

Auffan, M., Rose, J., Bottero, J.-Y., Lowry, G.V., Jolivet, J.-P., Wiesner, M.R., 2009. Towards a definition of inorganic nanoparticles from an environmental, health and safety perspective. Nat. Nanotechnol. 4, 634–641. https://doi.org/10.1038/nnano.2009.242.

Augustine, R., Hasan, A., Primavera, R., Wilson, R.J., Thakor, A.S., Kevadiya, B.D., 2020. Cellular uptake and retention of nanoparticles: insights on particle properties and interaction with cellular components. Mater. Today Commun. 25, 101692 https://doi.org/10.1016/j.mtcomm.2020.101692.

Bandín, I., Olveira, J.G., Borrego, J.J., Dopazo, C.P., Barja, J.L., 2006. Susceptibility of the fish cell line SAF-1 to betanodavirus. J. Fish Dis. 29, 633–636. https://doi.org/10.1111/j.1365-2761.2006.00757.x.

Barreto, A., Luis, L.G., Paíga, P., Santos, L.H.M.L.M., Delerue-Matos, C., Soares, A.M.V.M., Hylland, K., Loureiro, S., Oliveira, M., 2018. A multibiomarker approach highlights effects induced by the human pharmaceutical gemfibrozil to gilthead seabream Sparus aurata. Aquat. Toxicol. 200, 266–274. https://doi.org/10.1016/j.aquatox.2018.05.012.

Bejar, J., Borrego, J.J., Alvarez, M.C., 1997. A continuous cell line from the cultured marine fish gilt-head seabream (Sparus aurata L.). Aquaculture 150, 143–153. https://doi.org/10.1016/S0044-8486(96)01469-X.

Bermejo-Nogales, A., Fernández-Cruz, M.L., Navas, J.M., 2017. Fish cell lines as a tool for the ecotoxicity assessment and ranking of engineered nanomaterials. Regul. Toxicol. Pharmacol. 90, 297–307. https://doi.org/10.1016/j.yrtph.2017.09.029.

Boháčková, J., Havlíčková, L., Semerád, J., Titov, I., Trhlíková, O., Beneš, H., Cajthaml, T., 2023. In vitro toxicity assessment of polyethylene terephthalate and polyvinyl chloride microplastics using three cell lines from rainbow trout (Oncorhynchus mykiss). Chemosphere 312, 136996. https://doi.org/10.1016/j.chemosphere.2022.136996.

Bols, N.C., Dayeh, V.R., Lee, L.E.J., Schirmer, K., 2005. Use of fish cell lines in the toxicology and ecotoxicology of fish. Piscine cell lines in environmental toxicology. In: Biochemistry and Molecular Biology of Fishes, pp. 43–84. https://doi.org/10.1016/S1873-0140(05)80005-0.

Boudreau, N., Sympson, C.J., Werb, Z., Bissell, M.J., 1995. Suppression of ICE and apoptosis in mammary epithelial cells by extracellular matrix. Science 267, 891–893. https://doi.org/10.1126/SCIENCE.7531366.

Brandts, I., Solà, R., Garcia-Ordoñez, M., Gella, A., Quintana, A., Martin, B., Esteve-Codina, A., Teles, M., Roher, N., 2023. Polystyrene nanoplastics target lysosomes interfering with lipid metabolism through the PPAR system and affecting macrophage functionalization. Environ. Sci. Nano 10. https://doi.org/10.1039/d2en01077a.

Caminada, D., Escher, C., Fent, K., 2006. Cytotoxicity of pharmaceuticals found in aquatic systems: comparison of PLHC-1 and RTG-2 fish cell lines. Aquat. Toxicol. 79, 114–123. https://doi.org/10.1016/j.aquatox.2006.05.010.

Cance, W.G., Golubovskaya, V.M., 2008. Focal adhesion kinase versus p53: apoptosis or survival? Sci. Signal. 1 https://doi.org/10.1126/stke.120pe22.

Carlson, M., 2023. org.Dr.eg.db: Genome Wide Annotation for Zebrafish. R Package Version 3.17.0.

Cedervall, T., Lynch, I., Lindman, S., Berggård, T., Thulin, E., Nilsson, H., Dawson, K.A., Linse, S., 2007. Understanding the nanoparticle–protein corona using methods to quantify exchange rates and affinities of proteins for nanoparticles. Proc. Natl. Acad. Sci. 104, 2050–2055. https://doi.org/10.1073/pnas.0608582104.

Crouch, D.H., Fincham, V.J., Frame, M.C., 1996. Targeted proteolysis of the focal adhesion kinase pp125(FAK) during c-Myc-induced apoptosis is suppressed by integrin signalling. Oncogene 12, 2689–2696.

de Haan, W.P., Sanchez-Vidal, A., Canals, M., 2019. Floating microplastics and aggregate formation in the Western Mediterranean Sea. Mar. Pollut. Bull. 140, 523–535. https://doi.org/10.1016/j.marpolbul.2019.01.053.

de Sá, L.C., Oliveira, M., Ribeiro, F., Rocha, T.L., Futter, M.N., 2018. Studies of the effects of microplastics on aquatic organisms: what do we know and where should we focus our efforts in the future? Sci. Total Environ. 645, 1029–1039. https://doi.org/10.1016/j.scitotenv.2018.07.207.

Domenech, J., de Britto, M., Velázquez, A., Pastor, S., Hernández, A., Marcos, R., Cortés, C., 2021. Long-term effects of polystyrene nanoplastics in human intestinal Caco-2 cells. Biomolecules 11. https://doi.org/10.3390/biom11101442.

Drasler, B., Sayre, P., Steinhäuser, K.G., Petri-Fink, A., Rothen-Rutishauser, B., 2017. In vitro approaches to assess the hazard of nanomaterials. NanoImpact 8, 99–116. https://doi.org/10.1016/j.impact.2017.08.002.

Du, Y., Liu, X., Dong, X., Yin, Z., 2022. A review on marine plastisphere: biodiversity, formation, and role in degradation. Comput. Struct. Biotechnol. J. 20, 975–988. https://doi.org/10.1016/j.csbj.2022.02.008.

Durinck, S., Spellman, P.T., Birney, E., Huber, W., 2009. Mapping identifiers for the integration of genomic datasets with the R/Bioconductor package biomaRt. Nat. Protoc. 4, 1184–1191. https://doi.org/10.1038/nprot.2009.97.

El Aamri, F., Real, F., Acosta, F., Acosta, B., Valdivia, J., Ramos-Vivas, J., Padilla, D., 2012. In vitro study of adherence, invasion, and persistence of streptococcus iniae in fibroblastic-like fish cell line SAF-1. J. Aquat. Anim. Health 24, 165–170. https://doi.org/10.1080/08997659.2012.675928.

Eriksen, M., Cowger, W., Erdle, L.M., Coffin, S., Villarrubia-Gómez, P., Moore, C.J., Carpenter, E.J., Day, R.H., Thiel, M., Wilcox, C., 2023. A growing plastic smog, now estimated to be over 170 trillion plastic particles afloat in the world's oceans—urgent solutions required. PloS One 18, e0281596. https://doi.org/10.1371/journal.pone.0281596.

Evan, G.I., Brown, L., Whyte, M., Harrington, E., 1995. Apoptosis and the cell cycle. Curr. Opin. Cell Biol. 7, 825–834. https://doi.org/10.1016/0955-0674(95)80066-2.

Fazlollahi, F., Angelow, S., Yacobi, N.R., Marchelletta, R., Yu, A.S.L., Hamm-Alvarez, S. F., Borok, Z., Kim, K.-J., Crandall, E.D., 2011. Polystyrene nanoparticle trafficking across MDCK-II. Nanomed. Nanotechnol. Biol. Med. 7, 588–594. https://doi.org/10.1016/j.nano.2011.01.008.

Feng, Y., Tu, C., Li, R., Wu, D., Yang, J., Xia, Y., Peijnenburg, W.J.G.M., Luo, Y., 2023. A systematic review of the impacts of exposure to micro- and nano-plastics on human tissue accumulation and health. Eco-Environment Heal. 2, 195–207. https://doi.org/10.1016/j.eehl.2023.08.002.

Fent, K., 2001. Fish cell lines as versatile tools in ecotoxicology: assessment of cytotoxicity, cytochrome P4501A induction potential and estrogenic activity of chemicals and environmental samples. Toxicol. Vitr. 15, 477–488. https://doi.org/10.1016/S0887-2333(01)00053-4.

Forte, M., Iachetta, G., Tussellino, M., Carotenuto, R., Prisco, M., De Falco, M., Laforgia, V., Valiante, S., 2016. Polystyrene nanoparticles internalization in human gastric adenocarcinoma cells. Toxicol. Vitr. 31, 126–136. https://doi.org/10.1016/j.tiv.2015.11.006.

Franco, M.E., Lavado, R., 2019. Applicability of in vitro methods in evaluating the biotransformation of polycyclic aromatic hydrocarbons (PAHs) in fish: advances and challenges. Sci. Total Environ. 671, 685–695. https://doi.org/10.1016/j.scitotenv.2019.03.394.

Frisch, S.M., Ruoslahti, E., 1997. Integrins and anoikis. Curr. Opin. Cell Biol. 9, 701–706. https://doi.org/10.1016/S0955-0674(97)80124-X.

Galbis-Martínez, L., Fernández-Cruz, M.L., Alte, L., Valdehita, A., Rucandio, I., Navas, J. M., 2018. Development of a new tool for the long term in vitro ecotoxicity testing of nanomaterials using a rainbow-trout cell line (RTL-W1). Toxicol. Vitr. 50, 305–317. https://doi.org/10.1016/j.tiv.2018.04.007.

García Rellán, A., Vázquez Ares, D., Vázquez Brea, C., Francisco López, A., Bello Bugallo, P.M., 2023. Sources, sinks and transformations of plastics in our oceans: review, management strategies and modelling. Sci. Total Environ. 854, 158745 https://doi.org/10.1016/j.scitotenv.2022.158745.

Gasch, A.P., Spellman, P.T., Kao, C.M., Carmel-Harel, O., Eisen, M.B., Storz, G., Botstein, D., Brown, P.O., 2000. Genomic expression programs in the response of yeast cells to environmental changes. Mol. Biol. Cell 11, 4241–4257. https://doi.org/10.1091/mbc.11.12.4241.

Gavathiotis, E., Suzuki, M., Davis, M.L., Pitter, K., Bird, G.H., Katz, S.G., Tu, H.-C., Kim, H., Cheng, E.H.Y., Tjandra, N., Walensky, L.D., 2008. BAX activation is initiated at a novel interaction site. Nature 455, 1076–1081. https://doi.org/10.1038/nature07396.

Gervais, F.G., Thornberry, N.A., Ruffolo, S.C., Nicholson, D.W., Roy, S., 1998. Caspases cleave focal adhesion kinase during apoptosis to generate a FRNK-like polypeptide. J. Biol. Chem. 273, 17102–17108. https://doi.org/10.1074/jbc.273.27.17102.

Gigault, J., Ter Halle, A., Baudrimont, M., Pascal, P.-Y., Gauffre, F., Phi, T.-L., El Hadri, H., Grassl, B., Reynaud, S., 2018. Current opinion: what is a nanoplastic? Environ. Pollut. 235, 1030–1034. https://doi.org/10.1016/j.envpol.2018.01.024.

Gonçalves, J.M., Bebianno, M.J., 2021. Nanoplastics impact on marine biota: a review. Environ. Pollut. 273, 116426 https://doi.org/10.1016/j.envpol.2021.116426.

Gopinath, P.M., Saranya, V., Vijayakumar, S., Mythili Meera, M., Ruprekha, S., Kunal, R., Pranay, A., Thomas, J., Mukherjee, A., Chandrasekaran, N., 2019. Assessment on interactive prospectives of nanoplastics with plasma proteins and the toxicological impacts of virgin, coronated and environmentally released-nanoplastics. Sci. Rep. 9, 8860. https://doi.org/10.1038/s41598-019-45139-6.

Goswami, M., Yashwanth, B.S., Trudeau, V., Lakra, W.S., 2022. Role and relevance of fish cell lines in advanced in vitro research. Mol. Biol. Rep. 49, 2393–2411. https://doi.org/10.1007/s11033-021-06997-4.

Guarnieri, D., Guaccio, A., Fusco, S., Netti, P.A., 2011. Effect of serum proteins on polystyrene nanoparticle uptake and intracellular trafficking in endothelial cells. J. Nanopart. Res. 13, 4295–4309. https://doi.org/10.1007/s11051-011-0375-2.

Guerrera, M.C., Aragona, M., Porcino, C., Fazio, F., Laurà, R., Levanti, M., Montalbano, G., Germanà, G., Abbate, F., Germanà, A., 2021. Micro and nano plastics distribution in fish as model organisms: histopathology, blood response and bioaccumulation in different organs. Appl. Sci. 11, 5768. https://doi.org/10.3390/app11155768.

Guimarães, A.T.B., Estrela, F.N., Pereira, P.S., de Andrade Vieira, J.E., de Lima Rodrigues, A.S., Silva, F.G., Malafaia, G., 2021. Toxicity of polystyrene nanoplastics in Ctenopharyngodon idella juveniles: a genotoxic, mutagenic and cytotoxic

perspective. Sci. Total Environ. 752, 141937 https://doi.org/10.1016/j.scitotenv.2020.141937.

Guo, J.-J., Huang, X.-P., Xiang, L., Wang, Y.-Z., Li, Y.-W., Li, H., Cai, Q.-Y., Mo, C.-H., Wong, M.-H., 2020. Source, migration and toxicology of microplastics in soil. Environ. Int. 137, 105263 https://doi.org/10.1016/j.envint.2019.105263.

Han, Y., Lian, F., Xiao, Z., Gu, S., Cao, X., Wang, Z., Xing, B., 2022. Potential toxicity of nanoplastics to fish and aquatic invertebrates: current understanding, mechanistic interpretation, and meta-analysis. J. Hazard. Mater. 427, 127870 https://doi.org/10.1016/j.jhazmat.2021.127870.

Han, H., Chen, J., Li, J., Correia, A., Bártolo, R., Shahbazi, M.A., Teesalu, T., Wang, S., Cui, W., Santos, H.A., 2023. Enhancing apoptosome assembly via mito-biomimetic lipid nanocarrier for cancer therapy. Adv. Funct. Mater. 33 https://doi.org/10.1002/adfm.202305316.

He, L., He, T., Farrar, S., Ji, L., Liu, T., Ma, X., 2017. Antioxidants maintain cellular redox homeostasis by elimination of reactive oxygen species. Cell. Physiol. Biochem. 44, 532–553. https://doi.org/10.1159/000485089.

He, Y., Li, J., Chen, J., Miao, X., Li, G., He, Q., Xu, H., Li, H., Wei, Y., 2020. Cytotoxic effects of polystyrene nanoplastics with different surface functionalization on human HepG2 cells. Sci. Total Environ. 723, 138180 https://doi.org/10.1016/j.scitotenv.2020.138180.

Hernández-Moreno, D., Blázquez, M., Navas, J., Fernández-Cruz, M., 2022. Fish cell lines as screening tools to predict acute toxicity to fish of biocidal active substances and their relevant environmental metabolites. Aquat. Toxicol. 242, 106020 https://doi.org/10.1016/j.aquatox.2021.106020.

Herwig, S., Strauss, M., 1997. The retinoblastoma protein: a master regulator of cell cycle, differentiation and apoptosis. Eur. J. Biochem. 246, 581–601. https://doi.org/10.1111/j.1432-1033.1997.t01-2-00581.x.

Hesler, M., Aengenheister, L., Ellinger, B., Drexel, R., Straskraba, S., Jost, C., Wagner, S., Meier, F., von Briesen, H., Büchel, C., Wick, P., Buerki-Thurnherr, T., Kohl, Y., 2019. Multi-endpoint toxicological assessment of polystyrene nano- and microparticles in different biological models in vitro. Toxicol. Vitr. 61, 104610 https://doi.org/10.1016/j.tiv.2019.104610.

Hollóczki, O., Gehrke, S., 2019. Nanoplastics can change the secondary structure of proteins. Sci. Rep. 9, 16013 https://doi.org/10.1038/s41598-019-52495-w.

Hu, H., Tian, M., Ding, C., Yu, S., 2019. The C/EBP homologous protein (CHOP) transcription factor functions in endoplasmic reticulum stress-induced apoptosis and microbial infection. Front. Immunol. 10, 1–13. https://doi.org/10.3389/fimmu.2018.03083.

Hungerford, J.E., Compton, M.T., Matter, M.L., Hoffstrom, B.G., Otey, C.A., 1996. Inhibition of pp125FAK in cultured fibroblasts results in apoptosis. J. Cell Biol. 135, 1383–1390. https://doi.org/10.1083/jcb.135.5.1383.

Jan, R., Chaudhry, G.-S., 2019. Understanding apoptosis and apoptotic pathways targeted cancer therapeutics. Adv. Pharm. Bull. 9, 205–218. https://doi.org/10.15171/apb.2019.024.

Jeong, C.-B., Kang, H.-M., Lee, Y.H., Kim, M.-S., Lee, Jin-Sol, Seo, J.S., Wang, M., Lee, Jae-Seong, 2018. Nanoplastic ingestion enhances toxicity of persistent organic pollutants (POPs) in the monogonont rotifer Brachionus koreanus via multixenobiotic resistance (MXR) disruption. Environ. Sci. Technol. 52, 11411–11418. https://doi.org/10.1021/acs.est.8b03211.

Ji, Y., Wang, Y., Shen, D., Kang, Q., Chen, L., 2021. Mucin corona delays intracellular trafficking and alleviates cytotoxicity of nanoplastic-benzopyrene combined contaminant. J. Hazard. Mater. 406 https://doi.org/10.1016/j.jhazmat.2020.124306.

Johnston, H.J., Semmler-Behnke, M., Brown, D.M., Kreyling, W., Tran, L., Stone, V., 2010. Evaluating the uptake and intracellular fate of polystyrene nanoparticles by primary and hepatocyte cell lines in vitro. Toxicol. Appl. Pharmacol. 242, 66–78. https://doi.org/10.1016/j.taap.2009.09.015.

Katsumiti, A., Cajaraville, M.P., 2019. Ecotoxicology of nanoparticles in aquatic systems. In: Blasco, J., Corsi, I. (Eds.), Ecotoxicology of Nanoparticles in Aquatic Systems, pp. 1–260. https://doi.org/10.1201/9781315158761.

Kevadiya, B.D., Ottemann, B.M., Thomas, M. Ben, Mukadam, I., Nigam, S., McMillan, J., Gorantla, S., Bronich, T.K., Edagwa, B., Gendelman, H.E., 2019. Neurotheranostics as personalized medicines. Adv. Drug Deliv. Rev. 148, 252–289. https://doi.org/10.1016/j.addr.2018.10.011.

Khan, A., Jia, Z., 2023. Recent insights into uptake, toxicity, and molecular targets of microplastics and nanoplastics relevant to human health impacts. iScience 26, 106061. https://doi.org/10.1016/j.isci.2023.106061.

Kibria, M.G., Masuk, N.I., Safayet, R., Nguyen, H.Q., Mourshed, M., 2023. Plastic waste: challenges and opportunities to mitigate pollution and effective management. Int. J. Environ. Res. 17, 20. https://doi.org/10.1007/s41742-023-00507-z.

Kihara, S., Ashenden, A., Kaur, M., Glasson, J., Ghosh, S., van der Heijden, N., Brooks, A. E.S., Mata, J.P., Holt, S., Domigan, L.J., Köper, I., McGillivray, D.J., 2021. Cellular interactions with polystyrene nanoplastics—the role of particle size and protein corona. Biointerphases 16. https://doi.org/10.1116/6.0001124.

Kik, K., Bukowska, B., Sicińska, P., 2020. Polystyrene nanoparticles: sources, occurrence in the environment, distribution in tissues, accumulation and toxicity to various organisms. Environ. Pollut. 262, 114297 https://doi.org/10.1016/j.envpol.2020.114297.

Kim, H.-E., Du, F., Fang, M., Wang, X., 2005. Formation of apoptosome is initiated by cytochrome c -induced dATP hydrolysis and subsequent nucleotide exchange on Apaf-1. Proc. Natl. Acad. Sci. 102, 17545–17550. https://doi.org/10.1073/pnas.0507900102.

Kim, H.J., Olesen, N.J., Dale, O.B., Kim, Y.C., Jung, T.S., Vendramin, N., Kwon, S.R., 2023. Pathogenicity of two lineages of infectious hematopoietic necrosis virus (IHNV) to farmed rainbow trout (Oncorhynchus mykiss) in South Korea. Virus Res. 332, 199133 https://doi.org/10.1016/j.virusres.2023.199133.

Kuida, K., 2000. Caspase-9. Int. J. Biochem. Cell Biol. 32, 121–124. https://doi.org/10.1016/S1357-2725(99)00024-2.

Langner, S., Rakers, S., Ciba, P., Petschnik, A., Rapoport, D., Kruse, C., 2011. New cell line from adipopancreatic tissue of Atlantic herring Clupea harengus. Aquat. Biol. 11, 271–278. https://doi.org/10.3354/ab00317.

Law, K.L., 2017. Plastics in the marine environment. Ann. Rev. Mar. Sci. 9, 205–229. https://doi.org/10.1146/annurev-marine-010816-060409.

Lebreton, L., Andrady, A., 2019. Future scenarios of global plastic waste generation and disposal. Palgrave Commun. 5 https://doi.org/10.1057/s41599-018-0212-7.

Lesniak, A., Campbell, A., Monopoli, M.P., Lynch, I., Salvati, A., Dawson, K.A., 2010. Serum heat inactivation affects protein corona composition and nanoparticle uptake. Biomaterials 31, 9511–9518. https://doi.org/10.1016/j.biomaterials.2010.09.049.

Li, B., Dewey, C.N., 2011. RSEM: accurate transcript quantification from RNA-Seq data with or without a reference genome. BMC Bioinformatics 12. https://doi.org/10.1186/1471-2105-12-323.

Li, L., Sun, S., Tan, L., Wang, Y., Wang, L., Zhang, Z., Zhang, L., 2019. Correction to "polystyrene nanoparticles reduced ROS and inhibited ferroptosis by triggering lysosome stress and TFEB nucleus translocation in a size-dependent manner". Nano Lett. 19, 9170. https://doi.org/10.1021/acs.nanolett.9b04770.

Li, P., Wang, X., Su, M., Zou, X., Duan, L., Zhang, H., 2021. Characteristics of plastic pollution in the environment: a review. Bull. Environ. Contam. Toxicol. 107, 577–584. https://doi.org/10.1007/s00128-020-02820-1.

Li, Z., Huang, Y., Zhong, Y., Liang, B., Yang, X., Wang, Q., Sui, H., Huang, Z., 2023. Impact of food matrices on the characteristics and cellular toxicities of ingested nanoplastics in a simulated digestive tract. Food Chem. Toxicol. 179, 113984 https://doi.org/10.1016/j.fct.2023.113984.

Lisser, D., Vo, N.T.K., DeWitte-Orr, S.J., 2017. Delineating the roles of cellular and innate antiviral immune parameters mediating ranavirus susceptibility using rainbow trout cell lines. Virus Res. 238, 114–123. https://doi.org/10.1016/j.virusres.2017.06.008.

Liu, L., Xu, K., Zhang, B., Ye, Y., Zhang, Q., Jiang, W., 2021. Cellular internalization and release of polystyrene microplastics and nanoplastics. Sci. Total Environ. 779, 146523 https://doi.org/10.1016/j.scitotenv.2021.146523.

Love, M.I., Huber, W., Anders, S., 2014. Moderated estimation of fold change and dispersion for RNA-seq data with DESeq2. Genome Biol. 15, 550. https://doi.org/10.1186/s13059-014-0550-8.

Luo, W., Brouwer, C., 2013. Pathview: an R/Bioconductor package for pathway-based data integration and visualization. Bioinformatics 29, 1830–1831. https://doi.org/10.1093/bioinformatics/btt285.

Magni, S., Gagné, F., André, C., Della Torre, C., Auclair, J., Hanana, H., Parenti, C.C., Bonasoro, F., Binelli, A., 2018. Evaluation of uptake and chronic toxicity of virgin polystyrene microbeads in freshwater zebra mussel Dreissena polymorpha (Mollusca: Bivalia). Sci. Total Environ. 631–632, 778–788. https://doi.org/10.1016/j.scitotenv.2018.03.075.

Miccoli, A., Pianese, V., Bidoli, C., Fausto, A.M., Scapigliati, G., Picchietti, S., 2024. Transcriptome profiling of microdissected cortex and medulla unravels functional regionalization in the European sea bass Dicentrarchus labrax thymus. Fish Shellfish Immunol. 145, 109319 https://doi.org/10.1016/j.fsi.2023.109319.

Moné, M.J., Pallocca, G., Escher, S.E., Exner, T., Herzler, M., Bennekou, S.H., Kamp, H., Kroese, E.D., Leist, M., Steger-Hartmann, T., van de Water, B., 2020. Setting the stage for next-generation risk assessment with non-animal approaches: the EU-ToxRisk project experience. Arch. Toxicol. 94, 3581–3592. https://doi.org/10.1007/s00204-020-02866-4.

Morcillo, P., Chaves-Pozo, E., Meseguer, J., Esteban, M.Á., Cuesta, A., 2017. Establishment of a new teleost brain cell line (DLB-1) from the European sea bass and its use to study metal toxicology. Toxicol. Vitr. 38, 91–100. https://doi.org/10.1016/j.tiv.2016.10.005.

Mylvaganam, S., Freeman, S.A., Grinstein, S., 2021. The cytoskeleton in phagocytosis and macropinocytosis. Curr. Biol. 31, R619–R632. https://doi.org/10.1016/j.cub.2021.01.036.

Nardi, A., Pittura, L., D'Errico, G., Cesaroni, D., Mongera, F., Gorbi, S., Benedetti, M., Regoli, F., 2024. Cellular effects of microplastics are influenced by their dimension: mechanistic relationships and integrated criteria for particles definition. Environ. Pollut. 344, 123327 https://doi.org/10.1016/j.envpol.2024.123327.

OECD, 2023. Towards Eliminating Plastic Pollution by 2040 a Policy Scenario Analysis.

Okumura, N., Hashimoto, K., Kitahara, M., Okuda, H., Ueda, E., Watanabe, K., Nakahara, M., Sato, T., Kinoshita, S., Tourtas, T., Schlötzer-Schrehardt, U., Kruse, F., Koizumi, N., 2017. Activation of TGF-β signaling induces cell death via the unfolded protein response in Fuchs endothelial corneal dystrophy. Sci. Rep. 7, 6801. https://doi.org/10.1038/s41598-017-06924-3.

Otey, C.A., 1996. Pp125FAK in the focal adhesion. Int. Rev. Cytol. 167, 161–183. https://doi.org/10.1016/s0074-7696(08)61347-9.

Pang, M., Wang, Y., Tang, Y., Dai, J., Tong, J., Jin, G., 2021. Transcriptome sequencing and metabolite analysis reveal the toxic effects of nanoplastics on tilapia after exposure to polystyrene. Environ. Pollut. 277, 116860 https://doi.org/10.1016/j.envpol.2021.116860.

Pannetier, P., Fuster, L., Clérandeau, C., Lacroix, C., Gourves, P.-Y., Cachot, J., Morin, B., 2018. Usefulness of RTL-W1 and OLCAB-e3 fish cell lines and multiple endpoint measurements for toxicity evaluation of unknown or complex mixture of chemicals. Ecotoxicol. Environ. Saf. 150, 40–48. https://doi.org/10.1016/j.ecoenv.2017.12.027.

Pannetier, P., Morin, B., Le Bihanic, F., Dubreil, L., Clérandeau, C., Chouvellon, F., Van Arkel, K., Danion, M., Cachot, J., 2020. Environmental samples of microplastics induce significant toxic effects in fish larvae. Environ. Int. 134, 105047 https://doi.org/10.1016/j.envint.2019.105047.

Pantano, L., 2021. DEGreport: Report of DEG Analysis. R Package Version 1.36. https://doi.org/10.18129/B9.bioc.DEGreport.

Parra-Riofrio, G., Moreno, P., García-Rosado, E., Alonso, M.C., Uribe-Tapia, E., Abdala-Diaz, R.T., Bejar, J., 2023. Tetraselmis suecica and Porphyridium cruentum exopolysaccharides show anti-VHSV activity on RTG-2 cells. Aquac. Int. 31, 3145–3157. https://doi.org/10.1007/s10499-023-01202-8.

Pelletier, A.J., Kunicki, T., Ruggeri, Z.M., Quaranta, V., 1995. The activation state of the integrin αIIbβ3 affects outside-in signals leading to cell spreading and focal adhesion kinase phosphorylation. J. Biol. Chem. 270, 18133–18140. https://doi.org/10.1074/jbc.270.30.18133.

Peña-Blanco, A., García-Sáez, A.J., 2018. Bax, Bak and beyond — mitochondrial performance in apoptosis. FEBS J. 285, 416–431. https://doi.org/10.1111/febs.14186.

Peng, L., Fu, D., Qi, H., Lan, C.Q., Yu, H., Ge, C., 2020. Micro- and nano-plastics in marine environment: source, distribution and threats — a review. Sci. Total Environ. 698, 134254 https://doi.org/10.1016/j.scitotenv.2019.134254.

Perez-Prieto, S., Rodriguez-Saint-Jean, S., Garcia-Rosado, E., Castro, D., Alvarez, M., Borrego, J., 1999. Virus susceptibility of the fish cell line SAF-1 derived from gilt-head seabream. Dis. Aquat. Organ. 35, 149–153. https://doi.org/10.3354/dao035149.

Pham, P.H., Misk, E., Papazotos, F., Jones, G., Polinski, M.P., Contador, E., Russell, S., Garver, K.A., Lumsden, J.S., Bols, N.C., 2020. Screening of fish cell lines for piscine orthoreovirus-1 (PRV-1) amplification: identification of the non-supportive PRV-1 invitrome. Pathogens 9, 833. https://doi.org/10.3390/pathogens9100833.

Poma, A., Vecchiotti, G., Colafarina, S., Zarivi, O., Aloisi, M., Arrizza, L., Chichiriccò, G., Di Carlo, P., 2019. In vitro genotoxicity of polystyrene nanoparticles on the human fibroblast Hs27 cell line. Nanomaterials 9, 1299. https://doi.org/10.3390/nano9091299.

Qin, J., Xia, P.-F., Yuan, X.-Z., Wang, S.-G., 2022. Chlorine disinfection elevates the toxicity of polystyrene microplastics to human cells by inducing mitochondria-dependent apoptosis. J. Hazard. Mater. 425, 127842 https://doi.org/10.1016/j.jhazmat.2021.127842.

Rafael, M.S., Marques, C.L., Parameswaran, V., Cancela, M.L., Laizé, V., 2010. Fish bone-derived cell lines: an alternative in vitro cell system to study bone biology. J. Appl. Ichthyol. 26, 230–234. https://doi.org/10.1111/j.1439-0426.2010.01411.x.

Reimand, J., Isserlin, R., Voisin, V., Kucera, M., Tannus-Lopes, C., Rostamianfar, A., Wadi, L., Meyer, M., Wong, J., Xu, C., Merico, D., Bader, G.D., 2019. Pathway enrichment analysis and visualization of omics data using g:Profiler, GSEA, Cytoscape and EnrichmentMap. Nat. Protoc. 14, 482–517. https://doi.org/10.1038/s41596-018-0103-9.

Reinholz, J., Diesler, C., Schöttler, S., Kokkinopoulou, M., Ritz, S., Landfester, K., Mailänder, V., 2018. Protein machineries defining pathways of nanocarrier exocytosis and transcytosis. Acta Biomater. 71, 432–443. https://doi.org/10.1016/j.actbio.2018.03.006.

Rejman, J., Oberle, V., Zuhorn, I.S., Hoekstra, D., 2004. Size-dependent internalization of particles via the pathways of clathrin-and caveolae-mediated endocytosis. Biochem. J. 377, 159–169. https://doi.org/10.1042/BJ20031253.

Revel, M., Roman, C., Châtel, A., 2021. Is cell culture a suitable tool for the evaluation of micro- and nanoplastics ecotoxicity? Ecotoxicology 30, 421–430. https://doi.org/10.1007/s10646-021-02355-z.

Roshanzadeh, A., Park, S., Ganjbakhsh, S.E., Park, J., Lee, D.-H., Lee, S., Kim, E.-S., 2020. Surface charge-dependent cytotoxicity of plastic nanoparticles in alveolar cells under cyclic stretches. Nano Lett. 20, 7168–7176. https://doi.org/10.1021/acs.nanolett.0c02463.

Ruenraroengsak, P., Tetley, T.D., 2015. Differential bioreactivity of neutral, cationic and anionic polystyrene nanoparticles with cells from the human alveolar compartment: robust response of alveolar type 1 epithelial cells. Part. Fibre Toxicol. 12, 19. https://doi.org/10.1186/s12989-015-0091-7.

Ruiz, C.E., Manuguerra, S., Curcuraci, E., Santulli, A., Messina, C.M., 2020. Carbamazepine, cadmium chloride and polybrominated diphenyl ether-47, synergistically modulate the expression of antioxidants and cell cycle biomarkers, in the marine fish cell line SAF-1. Mar. Environ. Res. 154, 104844 https://doi.org/10.1016/j.marenvres.2019.104844.

Ruoslahti, E., Reed, J.C., 1994. Anchorage dependence, integrins, and apoptosis. Cell 77, 477–478. https://doi.org/10.1016/0092-8674(94)90209-7.

Sakata, S., Yan, Y.L., Satou, Y., Momoi, A., Ngo-Hazelett, P., Nozaki, M., Furutani-Seiki, M., Postlethwait, J.H., Yonehara, S., Sakamaki, K., 2007. Conserved function of caspase-8 in apoptosis during bony fish evolution. Gene 396, 134–148. https://doi.org/10.1016/j.gene.2007.03.010.

Santini, M.T., Rainaldi, G., Indovina, P.L., 2000. Apoptosis, cell adhesion and the extracellular matrix in the three-dimensional growth of multicellular tumor spheroids. Crit. Rev. Oncol. Hematol. 36, 75–87. https://doi.org/10.1016/S1040-8428(00)00078-0.

Schmidt, A., da Silva Brito, W.A., Singer, D., Mühl, M., Berner, J., Saadati, F., Wolff, C., Miebach, L., Wende, K., Bekeschus, S., 2023. Short- and long-term polystyrene nano- and microplastic exposure promotes oxidative stress and divergently affects skin cell architecture and Wnt/beta-catenin signaling. Part. Fibre Toxicol. 20, 1–23. https://doi.org/10.1186/s12989-023-00513-1.

Sendra, M., Saco, A., Yeste, M.P., Romero, A., Novoa, B., Figueras, A., 2020. Nanoplastics: from tissue accumulation to cell translocation into Mytilus galloprovincialis hemocytes. resilience of immune cells exposed to nanoplastics and nanoplastics plus Vibrio splendidus combination. J. Hazard. Mater. 388, 121788 https://doi.org/10.1016/j.jhazmat.2019.121788.

Sendra, M., Pereiro, P., Yeste, M.P., Mercado, L., Figueras, A., Novoa, B., 2021. Size matters: zebrafish (Danio rerio) as a model to study toxicity of nanoplastics from

cells to the whole organism. Environ. Pollut. 268, 115769 https://doi.org/10.1016/j.envpol.2020.115769.

Shi, C., Liu, Zhiqun, Yu, B., Zhang, Y., Yang, H., Han, Y., Wang, B., Liu, Zhiquan, Zhang, H., 2024. Emergence of nanoplastics in the aquatic environment and possible impacts on aquatic organisms. Sci. Total Environ. 906, 167404 https://doi.org/10.1016/j.scitotenv.2023.167404.

Subramanian, A., Tamayo, P., Mootha, V.K., Mukherjee, S., Ebert, B.L., Gillette, M.A., Paulovich, A., Pomeroy, S.L., Golub, T.R., Lander, E.S., Mesirov, J.P., 2005. Gene set enrichment analysis: a knowledge-based approach for interpreting genome-wide expression profiles. Proc. Natl. Acad. Sci. 102, 15545–15550. https://doi.org/10.1073/pnas.0506580102.

Sun, X.-D., Yuan, X.-Z., Jia, Y., Feng, L.-J., Zhu, F.-P., Dong, S.-S., Liu, J., Kong, X., Tian, H., Duan, J.-L., Ding, Z., Wang, S.-G., Xing, B., 2020. Differentially charged nanoplastics demonstrate distinct accumulation in Arabidopsis thaliana. Nat. Nanotechnol. 15, 755–760. https://doi.org/10.1038/s41565-020-0707-4.

Tarca, A.L., Draghici, S., Khatri, P., Hassan, S.S., Mittal, P., Kim, J.S., Kim, C.J., Kusanovic, J.P., Romero, R., 2009. A novel signaling pathway impact analysis. Bioinformatics 25, 75–82. https://doi.org/10.1093/bioinformatics/btn577.

Terhorst, A., Sandikci, A., Whittaker, C.A., Szórádi, T., Holt, L.J., Neurohr, G.E., Amon, A., 2023. The environmental stress response regulates ribosome content in cell cycle-arrested *S. cerevisiae*. Front. Cell Dev. Biol. 11 https://doi.org/10.3389/fcell.2023.1118766.

Turner, A., 2020. Foamed polystyrene in the marine environment: sources, additives, transport, behavior, and impacts. Environ. Sci. Technol. 54, 10411–10420. https://doi.org/10.1021/acs.est.0c03221.

Umamaheswari, S., Priyadarshinee, S., Kadirvelu, K., Ramesh, M., 2021. Polystyrene microplastics induce apoptosis via ROS-mediated p53 signaling pathway in zebrafish. Chem. Biol. Interact. 345, 109550 https://doi.org/10.1016/j.cbi.2021.109550.

Valero, Y., López-Vázquez, C., Souto, S., Olveira, J.G., Cuesta, A., Bandín, I., 2021. Differential nervous necrosis virus (NNV) replication in five putative susceptible cell lines. Pathogens 10, 1565. https://doi.org/10.3390/pathogens10121565.

Villalba, M., Pérez, V., Herrera, L., Stepke, C., Maldonado, N., Fredericksen, F., Yáñez, A., Olavarría, V.H., 2017. Infectious pancreatic necrosis virus infection of fish cell lines: preliminary analysis of gene expressions related to extracellular matrix remodeling and immunity. Vet. Immunol. Immunopathol. 193–194, 10–17. https://doi.org/10.1016/j.vetimm.2017.09.009.

Vo, N.T.K., Bufalino, M.R., Hartlen, K.D., Kitaev, V., Lee, L.E.J., 2014. Cytotoxicity evaluation of silica nanoparticles using fish cell lines. Vitr. Cell. Dev. Biol. - Anim. 50, 427–438. https://doi.org/10.1007/s11626-013-9720-3.

Walkey, C.D., Chan, W.C.W., 2012. Understanding and controlling the interaction of nanomaterials with proteins in a physiological environment. Chem. Soc. Rev. 41, 2780–2799. https://doi.org/10.1039/C1CS15233E.

Walkey, C.D., Olsen, J.B., Song, F., Liu, R., Guo, H., Olsen, D.W.H., Cohen, Y., Emili, A., Chan, W.C.W., 2014. Protein corona fingerprinting predicts the cellular interaction of gold and silver nanoparticles. ACS Nano 8, 2439–2455. https://doi.org/10.1021/nn406018q.

Wange, R.L., Brown, P.C., Davis-Bruno, K.L., 2021. Implementation of the principles of the 3Rs of animal testing at CDER: past, present and future. Regul. Toxicol. Pharmacol. 123, 104953 https://doi.org/10.1016/j.yrtph.2021.104953.

Wen, L.-P., Fahrni, J.A., Troie, S., Guan, J.-L., Orth, K., Rosen, G.D., 1997. Cleavage of focal adhesion kinase by caspases during apoptosis. J. Biol. Chem. 272, 26056–26061. https://doi.org/10.1074/jbc.272.41.26056.

Wolf, K., Quimby, M.C., 1962. Established eurythermic line of fish cells in vitro. Science 135, 1065–1066. https://doi.org/10.1126/science.135.3508.1065.

Wu, T., Hu, E., Xu, S., Chen, M., Guo, P., Dai, Z., Feng, T., Zhou, L., Tang, W., Zhan, L., Fu, X., Liu, S., Bo, X., Yu, G., 2021. clusterProfiler 4.0: a universal enrichment tool for interpreting omics data. Innovation 2, 100141. https://doi.org/10.1016/j.xinn.2021.100141.

Xu, M., Halimu, G., Zhang, Q., Song, Y., Fu, X., Li, Yongqiang, Li, Yansheng, Zhang, H., 2019. Internalization and toxicity: a preliminary study of effects of nanoplastic particles on human lung epithelial cell. Sci. Total Environ. 694 https://doi.org/10.1016/j.scitotenv.2019.133794.

Yang, T., Nowack, B., 2020. A meta-analysis of ecotoxicological hazard data for nanoplastics in marine and freshwater systems. Environ. Toxicol. Chem. 39, 2588–2598. https://doi.org/10.1002/etc.4887.

Yang, M., Wang, W.X., 2023. Recognition and movement of polystyrene nanoplastics in fish cells. Environ. Pollut. 316, 120627 https://doi.org/10.1016/j.envpol.2022.120627.

Ye, H.-Q., Chen, S.-L., Sha, Z.-X., Xu, M.-Y., 2006. Development and characterization of cell lines from heart, liver, spleen and head kidney of sea perch Lateolabrax japonicus. J. Fish Biol. 69, 115–126. https://doi.org/10.1111/j.1095-8649.2006.01155.x.

Yong, C., Valiyaveettil, S., Tang, B., 2020. Toxicity of microplastics and nanoplastics in mammalian systems. Int. J. Environ. Res. Public Health 17, 1509. https://doi.org/10.3390/ijerph17051509.

Yu, G., 2023. enrichplot: Visualization of Functional Enrichment Result. R Package Version 1.20.3.

Yu, G., He, Q.-Y., 2016. ReactomePA: an R/Bioconductor package for reactome pathway analysis and visualization. Mol. Biosyst. 12, 477–479. https://doi.org/10.1039/C5MB00663E.

Zaki, M.R.M., Aris, A.Z., 2022. An overview of the effects of nanoplastics on marine organisms. Sci. Total Environ. 831, 154757 https://doi.org/10.1016/j.scitotenv.2022.154757.

Zhang, Y., Wu, J.L.Y., Lazarovits, J., Chan, W.C.W., 2020. An analysis of the binding function and structural organization of the protein corona. J. Am. Chem. Soc. 142, 8827–8836. https://doi.org/10.1021/jacs.0c01853.

Zhao, J.Z., Xu, L.M., Ren, G.M., Shao, Y.Z., Liu, Q., Teng, C.B., Lu, T.Y., 2023a. Comparative transcriptome analysis of rainbow trout gonadal cells (RTG-2) infected with U and J genogroup infectious hematopoietic necrosis virus. Front. Microbiol. 13 https://doi.org/10.3389/fmicb.2022.1109606.

Zhao, X., Zhou, Y., Liang, C., Song, J., Yu, S., Liao, G., Zou, P., Tang, K.H.D., Wu, C., 2023b. Airborne microplastics: occurrence, sources, fate, risks and mitigation. Sci. Total Environ. 858, 159943 https://doi.org/10.1016/j.scitotenv.2022.159943.

Zhou, Y., He, G., Jiang, H., Pan, K., Liu, W., 2023. Nanoplastics induces oxidative stress and triggers lysosome-associated immune-defensive cell death in the earthworm Eisenia fetida. Environ. Int. 174, 107899 https://doi.org/10.1016/j.envint.2023.107899.

Zhu, A., Ibrahim, J.G., Love, M.I., 2019. Heavy-tailed prior distributions for sequence count data: removing the noise and preserving large differences. Bioinformatics 35, 2084–2092. https://doi.org/10.1093/bioinformatics/bty895.

Zhu, X., Wang, C., Duan, X., Liang, B., Genbo Xu, E., Huang, Z., 2023. Micro- and nanoplastics: a new cardiovascular risk factor? Environ. Int. 171, 107662 https://doi.org/10.1016/j.envint.2022.107662.